JOURNAL OF GEOPHYSICAL RESEARCH, VOL. 103, NO. D10, PAGES 11,263–11,288, MAY 27, 1998

Age of air in a zonally averaged two-dimensional model

Julio T. Bacmeister, David E. Siskind, and Michael E. Summers
Naval Research Laboratory, Washington, D.C.

Stephen D. Eckermann
Computational Physics Inc., Fairfax, Virginia

Abstract. The distribution of age-of-air in a two-dimensional, zonally averaged model of the atmosphere is examined. The age-of-air is determined from mixing ratios of a fictitious tracer with a linearly increasing tropospheric source. The impact of horizontal mixing is isolated by performing parallel calculations with and without horizontal mixing terms in the tracer evolution equation. We examine the evolution of the tracer over several model years, using different tropical heat sources as well as different amounts of planetary wave mixing and drag. Typical ages in the midstratosphere when horizontal mixing is included range from 3 to over 5 years, depending primarily on the strength of the model's prescribed tropical heat source. These values of age are within the range of observational estimates based on long-lived tracers with increasing tropospheric mixing ratios, such as HF, CO_2 and SF_6. Age determined from the horizontally unmixed tracer is reduced by 1 to 2 years. However, the evolution of the unmixed tracer is consistent with observed behavior of tropical water vapor oscillations in data from the HAlogen Occultation Experiment (HALOE). We found stronger than expected sensitivity of middle atmospheric age to prescribed heating in the tropical troposphere. This sensitivity in our model arises from small resulting changes to the residual vertical velocity in the tropics. These vertical velocity changes are in turn associated with net heating changes of 0.05-0.10 K d^{-1} in the tropical lower stratosphere. We argue that changes of this magnitude are within the uncertainties imposed by natural variations in the tropics.

1. Introduction

Accurate stratospheric measurements of long-lived tracers with increasing tropospheric mixing ratios have recently become available. These include SF_6 [*Elkins et al.* 1996; *Harnisch et al.*, 1996], CO_2 [*Schmidt and Khedim*, 1991; *Boering et al.*, 1994], and HF [*Russell et al.*, 1996]. Mixing ratios of such tropospheric source gases can be used to estimate the amount of time required for air parcels to travel from the troposphere to other locations in the atmosphere. This is done straightforwardly by comparing the mixing ratio of a tropospheric source gas at say 40 km altitude with a time history of its tropospheric mixing ratio. The time delay between the occurrence of a given mixing ratio in the troposphere and its appearance at higher altitudes is referred to as the "age" of the air mass, or simply age of air. This concept was first introduced by *Bischof et al.* [1985] to interpret differences in middle stratospheric and tropospheric mixing ratios of CO_2. Values of age determined in this way have been found to vary between 3 and 7 years in the midstratosphere (25-35 km) [*Schmidt and Khedim*, 1991]. *Hall and Prather* [1993] and more recently *Waugh et al.* [1997] examined the distribution of age in the stratosphere in three-dimensional general circulation model (GCM) simulations. Hall and Prather found ages between 3 and 4 years, while Waugh et al. found much older ages, from 6 years to 8–10 years depending on the parameterization of gravity waves which was employed. These studies used a single year's output from the GCMs to perform multiyear tracer simulations, so sensitivity of age to variations in dynamic or thermodynamic inputs to the GCMs were not assessed in detail. However, it is clearly of interest that such large differences in age exist between atmospheric models. *Hall and Plumb* [1994] examined the effects of the time behavior of tropospheric sources on determinations of stratospheric age.

Age-of-air in the middle atmosphere has also been defined as the time needed by a Lagrangian parcel to travel from the equatorial troposphere to another location in the middle atmosphere [e.g. *Rosenlof*, 1995]. Using parcels advected by a 2-D residual circulation inferred from United Kingdom Meteorological Office (UKMO) analyses of temperature, Rosenlof obtained

Paper number 98JD00277.
0148-0227/98/98JD-00277$09.00

Report Documentation Page

Form Approved
OMB No. 0704-0188

1. REPORT DATE	2. REPORT TYPE	3. DATES COVERED
MAY 1998		**00-00-1998 to 00-00-1998**

4. TITLE AND SUBTITLE	5a. CONTRACT NUMBER
Age of air in a zonally averaged two-dimensional model	5b. GRANT NUMBER
	5c. PROGRAM ELEMENT NUMBER
6. AUTHOR(S)	5d. PROJECT NUMBER
	5e. TASK NUMBER
	5f. WORK UNIT NUMBER
7. PERFORMING ORGANIZATION NAME(S) AND ADDRESS(ES) **Naval Research Laboratory,Washington,DC,20375**	8. PERFORMING ORGANIZATION REPORT NUMBER
9. SPONSORING/MONITORING AGENCY NAME(S) AND ADDRESS(ES)	10. SPONSOR/MONITOR'S ACRONYM(S)
	11. SPONSOR/MONITOR'S REPORT NUMBER(S)

12. DISTRIBUTION/AVAILABILITY STATEMENT
Approved for public release; distribution unlimited

13. SUPPLEMENTARY NOTES

14. ABSTRACT
see report

15. SUBJECT TERMS

16. SECURITY CLASSIFICATION OF:			17. LIMITATION OF ABSTRACT	18. NUMBER OF PAGES	19a. NAME OF RESPONSIBLE PERSON
a. REPORT **unclassified**	b. ABSTRACT **unclassified**	c. THIS PAGE **unclassified**	**Same as Report (SAR)**	**26**	

ages of less than 3 years in most of the stratosphere from Lagrangian travel times. Older values were obtained in the polar vortices. However, rapid horizontal motions in the atmosphere may produce significant differences between the Lagrangian age derived from 2-D circulations and the mean age of an ensemble of parcels in a fully 3-D flow . This reflects the fact that an air parcel in the 2-D circulation is actually composed of subelements which can have widely diverging reverse trajectories back to origin at the surface or injection into the stratosphere. *Hall and Plumb* [1994] introduced the concept of an "age spectrum" to encompass the variety of paths taken by air parcels between the troposphere and any particular point in the middle atmosphere. The mean-age, determined from long-lived tracers with linearly-increasing, tropospheric mixing ratios, is equal to the first moment of Hall and Plumb's age spectrum [*Hall and Plumb*, 1994]. However, irreversible horizontal mixing broadens the age spectrum so that its first moment is not equal to 2-D Lagrangian travel times. Thus we should expect age of air based on mixing ratio meaurements of long-lived trace gases to be different than Lagrangian ages based on the 2-D residual circulation.

The rate of transport from the troposphere into the middle atmosphere is determined by a balance between residual mean upward advection in the tropics and horizontal exchange of air between tropics and midlatitudes [e.g., *Boering et al.*, 1995; *Plumb*, 1996; *Volk et al.*, 1996]. Comparing age of air based on mixing ratio with age determined from Lagrangian parcel calculations will shed light on the realism of this balance in 2-D models. In zonally averaged 2-D models, irreversible horizontal mixing by atmospheric motions is typically represented as a diffusion process [e.g., *Plumb and Ko*, 1992; *Garcia et al.*, 1992]. The accuracy of horizontal mixing parameterizations is a major and well-recognized uncertainty in 2-D models.

On the other hand, the calculation of radiative net heating is generally regarded as a strong point of zonally averaged models, since it can be accurately calculated using a number of radiatively active gases. Therefore "tuning" of less well understood drag parameters in these models can, in principle, be accomplished by obtaining accurate simulations of wind and temperatures in the middle atmosphere in the presence of known distributions of radiatively active gases. When both correct drag and heating distributions are present in the model, a correct residual mean meridional circulation is guaranteed. This procedure is described by *Summers et al.* [1997] and *Siskind et al.* [1997] for the current Naval Research Laboratory (NRL) 2-D model.

Unfortunately, in the troposphere, nonradiative processes such as sensible surface heating and latent heating by water vapor condensation are the dominant inputs of heat. These processes are not generally well represented in zonally averaged 2-D models. These uncertainties would be of little interest to middle atmosphere modelers if their effects were restricted to the troposphere and lower stratosphere. However, in practice, we have found that model simulations of N_2O are sensitive to the strength of the specified heat source in the troposphere [*Summers et al.*, 1997]. Net heating rates in the tropical lower stratosphere are particularly sensitive to variations in infrared radiation welling up from below [e.g.. *Eluszkiewicz et al.*, 1996]. Also, it is now thought that vertical velocity at the tropical tropopause and in the lower stratosphere may be sensitive to or even controlled by lower stratospheric drag in midlatitudes [e.g., *Iwasaki*, 1992; *Rosenlof and Holton*, 1993; *Yulaeva et al.*, 1994; *Holton et al.*, 1995]. Thus, vertical velocity in the tropical lower stratosphere may be sensitive to numerous processes which are poorly or incompletely incorporated in 2-D models and as will be seen in this study, ascent rates through the lower stratosphere exert an important control on the age-of-air distribution in the middle atmosphere.

In this study we will present equilibrium distributions of age of air from a 2-D zonally averaged model of the atmosphere. We will use the NRL chemical/dynamical model [*Bacmeister et al.*, 1995; *Summers et al.*, 1997] to calculate the evolution of a fictitious long-lived tracer with a linearly increasing tropospheric mixing ratio. The mixing ratio of this tracer in the middle atmosphere will be used to obtain an equivalent age which should correspond to those obtained from long-lived trace gases such as SF_6 or CO_2. We will perform parallel age calculations using a tracer that is immune to horizontal mixing. Age from this "unmixed" tracer should resemble that which would be obtained from Lagrangian parcel calculations using the model residual circulation. There are two results from this study: (1) we demonstrate that 2-D models with parameterized planetary wave drag and mixing can obtain an approximately correct balance between upward advection in the tropics and horizontal mixing, and (2) we show that variations in prescribed heating of the tropical troposphere can lead to 1 to 2 year differences in the age of the model middle atmosphere. Point 2 is principally a modeling issue, since the tropospheric dynamics of a zonally averaged model of this kind are not realistic. Nevertheless, in exploring the sensitivity of the model to tropospheric heating we found that much of the middle atmosphere response to tropospheric heating variations was associated with small variations in the net heating of the tropical lower stratosphere. These variations in stratospheric net heating rates are within the uncertainties present in current radiative transfer calculations, due to, for example, the aerosol loading of the stratosphere.

The outline of this paper is as follows: In section 2 we briefly describe the formulation of the NRL 2-D model. We also describe the current state of model parameterizations for gravity wave drag, radiative transfer and other physical processes. In Section 3 we discuss results from several simulations. After presenting our baseline model climatology and age distribution in Sections 3.1 and 3.2, we will examine the impact of changing the planetary wave forcing (section 3.3) as well as the prescribed tropospheric heating (section 3.4) on model age-of-air. In section 4 we examine in more detail the response of the model meridional stream function to tropospheric heating parameters. Finally, in section 5 we summarize our results.

2. Description of Model and Numerical Experiments

A basic description of the dynamical portion of the NRL 2-D model is given by *Bacmeister et al.* [1995]. A brief summary of the model formulation is given here. The model is based on the Transformed Eulerian Mean (TEM) formulation [e.g., *Andrews et al.*, 1987]. Evolution equations for both zonally averaged potential temperature $\overline{\theta}$ and angular momentum $\overline{M}$ are solved:

$$\frac{\partial \overline{M}}{\partial t} + v^* \frac{\partial \overline{M}}{a \partial \phi} + w^* \frac{\partial \overline{M}}{\partial z} = X \tag{1a}$$

$$\frac{\partial \overline{\theta}}{\partial t} + v^* \frac{\partial \overline{\theta}}{a \partial \phi} + w^* \frac{\partial \overline{\theta}}{\partial z} = \mathcal{H} \tag{1b}$$

where zonally averaged angular momentum density is given by

$$\overline{M} = \overline{U} a \cos(\phi) + \Omega a^2 \cos^2(\phi) \tag{1c}$$

The numerical advection of $\overline{M}$ and $\overline{\theta}$ in (1a) and (1b) is accomplished using the scheme described by *Prather* [1986]. This scheme is highly nondiffusive and nondispersive and compares well with analytical solutions of the advection equation [*Prather*, 1986; *Rood*, 1987; *Shia et al.*, 1990] The term X denotes the total momentum forcing from all sources, including planetary wave Eliassen-Palm flux (EP-flux) divergence and gravity wave drag. The term $\mathcal{H}$ denotes the total thermodynamic forcing from all sources. The individual components of X and $\mathcal{H}$ are discussed below. All other symbols have the same meaning as in the work of *Andrews et al.* [1987] unless otherwise noted. The thermal wind relation is used with (1a) and (1b) to form a diagnostic elliptic equation for the residual meridional stream function ψ^*. The stream function is used to calculate the meridional and vertical residual velocities v^* and w^*. The integration of (1) and the solution of the meridional stream function equation including a geostrophic adjustment procedure is described by *Bacmeister et al.* [1995]. A major modification to the model, since *Bacmeister et al.* [1995], has been the addition of nonzero phase speed gravity waves to the gravity wave parameterization scheme. The current status of this and other parameterizations is described briefly next.

2.1. Momentum Forcing

The total momentum forcing X in the model can be broken down into components representing various physical processes,

$$X = D_{\mathrm{GW}} - \alpha_{\mathrm{Ray}} \overline{U} + \frac{\partial}{\partial z}\left(K_{\mathrm{mom}} \frac{\partial}{\partial z} \overline{U}\right) + \nabla \cdot \mathbf{F}_{\mathrm{PW}} \tag{2}$$

We now briefly describe each term in (2) and its current implementation in the model.

2.1.1. Gravity wave drag. The term D_{GW} represents drag produced by dissipating gravity waves. It is the only component of X that has been substantially modified since *Bacmeister et al.* [1995]. Drag and mixing from gravity waves with non-zero phase speeds have been added to obtain improved simulations of the mesosphere and upper stratosphere. To calculate drag and mixing caused by gravity waves with non-zero phase speeds, the parameterization uses a simplified, hydrostatic wave packet approach [*Bacmeister*, 1993; *Summers et al.*, 1997]. In the current simulations we specify time and latitiude independent surface amplitudes and phase speeds for a six wave spectrum of traveling gravity waves. These are given in Table 1. For drag from zero phase speed gravity waves the simple cubic law drag of *Bacmeister et al.* [1995] is retained. The scheme is described in more detail by *Summers et al.* [1997].

2.1.2. Rayleigh drag. The second term $\alpha_{\mathrm{Ray}} \overline{U}$ is an ad hoc Rayleigh-damping term. This is a crudely represented sink of angular momentum in the model stratosphere and troposphere. It is assumed to account for missing or imperfectly parameterized dynamics in the model, such as low-altitude orographic drag from large-amplitude mountain waves, or drag from high-wavenumber planetary waves. In the present study we will use α_{Ray}=0.01 d^{-1} for all calculations.

2.1.3. Vertical mixing. The third term $\partial_z(K_{\mathrm{mom}} \partial_z \overline{U})$ represents vertical redistribution of momentum by turbulent and molecular diffusion. Its effects on our simulations are negligible below the upper mesosphere, where large values of K_{mom} can be associated with gravity wave breaking and where large vertical shears in zonal winds may be present due to the effects of gravity wave drag.

2.1.4. Planetary Wave Drag. The term $\nabla \cdot \mathbf{F}_{\mathrm{PW}}$ represents EP-flux divergence associated with dissipating or breaking planetary waves. Planetary wave effects are parameterized as in the work of *Garcia* [1991], by forcing a time dependent, linear planetary wave model with zonal winds and temperatures from the zonally averaged TEM model. In this study we specify a time-independent, surface geopotential height perturbation for wavenumber 1 described by,

$$\Phi'(\phi, z_0, t) = \begin{cases} 0 & \text{if } \phi > 60° \\ Z_{\mathrm{NH}} \, |\sin 3\phi/2| & \text{if } 0° < \phi \le 60° \\ Z_{\mathrm{SH}} \, |\sin 3\phi/2| & \text{if } -60° < \phi \le 0° \\ 0 & \text{if } \phi < -60° \end{cases}$$

Table 1. Parameters for nonzero phase speed gravity waves used in all simulations discussed in this study. Column 1 gives wave phase speed. Column 2 gives peak vertical displacement amplitude associated with the waves at the launch altitude of ≈5.0 km. Column 3 gives the number of wave packets with these phase speeds and amplitudes encountered around a latitude band.

Phase Speed m s^{-1}	Amplitude m	Number per Band
+20	40.0	5.0
−20	40.0	5.0
+40	30.0	3.0
−40	30.0	3.0
+40	15.0	3.0
−40	15.0	3.0

Table 2. Experiments to be discussed in the text. Column 1 indicates the number of the experiment in the text. Column 2 gives the magnitude of the prescribed tropospheric heating used in the experiment. Column 3 indicates whether inputs to the thermodynamic forcing, such as O_3 or NMC surface temperatures, have been "symmetrized" with respect to hemisphere and season. Columns 4 and 5 indicate the amplitude of the planetary wave forcing in the northern and southern hemispheres. Experiment 1 represents the baseline simulation. Results for experiment 2 are similar in many respects to those for experiment 1, except that hemispheric asymmetries are supressed. In experiments 2, 3, and 4, symmetric planetary wave forcing amplitudes are varied, while tropospheric heating magnitude $\mathcal{H}_0$ is held fixed. In experiments 5 and 6, asymmetric planetary wave forcing amplitudes equal to those in the baseline simulation (experiment 1) are used, while the magnitude of prescribed tropospheric heating $\mathcal{H}_0$ is varied. In experiment 7, the tropospheric heating is the same as in experiment 1, but a small $\sim$0.3 K d^{-1} heat source centered at 25 km is added.

Experiment	$\mathcal{H}_0$ K d^{-1}	Inputs to $\mathcal{H}$	Z_{NH} m	Z_{SH} m
		Baseline simulation		
1	3.0	asymmetric	350	175
		Vary Planetary Waves With Fixed $\mathcal{H}_0$		
2	3.0	symmetric	250	250
3	3.0	symmetric	125	125
4	3.0	symmetric	350	350
		Vary $\mathcal{H}_0$ *With Fixed Planetary Waves*		
5	2.0	asymmetric	350	175
6	4.0	asymmetric	350	175
		Add Stratospheric Heating		
7	3.0 + $\mathcal{H}_{strat}$	asymmetric	350	175

We retain the possibility to select different surface forcing amplitudes in the southern and northern hemispheres as a crude way of modeling observed hemispheric asymmetries in planetary wave activity. Table 2 gives values of Z_{SH} and Z_{NH} and other parameters for each of the seven experiments discussed in this study. Earlier studies have used $Z_{SH} \approx 0.5 Z_{NH}$ to obtain reasonable hemispheric asymmetries in such features as wintertime trace gas distributions within the polar vortices [*Garcia et al.*, 1992; *Bacmeister et al.*, 1995]. The planetary wave EP-flux divergence is also used to calculate a mixing coefficient K_{PW} to represent rapid isentropic horizontal mixing by breaking planetary waves, thought to be the most important cause of rapid horizontal mixing in the stratosphere [e.g., *McIntyre and Palmer*, 1983]. A more detailed description of the planetary wave model is given by *Bacmeister et al.* [1995].

2.2. Thermodynamic Forcing

The contributions to the thermodynamic forcing $\mathcal{H}$ in (1b) can also be broken down into those from a number of different physical processes,

$$\mathcal{H} = \mathcal{H}_{gas} + \mathcal{H}_{latent} + \mathcal{H}_{strat} - \alpha_{bdy}(\overline{\theta} - \overline{\theta}_{NCEP}) + \frac{\partial}{\partial z}\left(K_{thrm}\frac{\partial}{\partial z}\overline{\theta}\right) \quad (3)$$

The significance of each term and its current parameterization is described below.

2.2.1. Radiative transfer. The first term $\mathcal{H}_{gas}$ is the net heating due to exchange of solar and terrestrial radiation by gases in the atmosphere. We use two radiative transfer parameterizations to calculate infrared heating and cooling in different layers of the atmosphere. Climatological O_3, CO_2, and H_2O are used. Details are discussed by *Summers et al.* [1997].

2.2.2. Prescribed tropospheric or "latent" heating. The second term $\mathcal{H}_{latent}$ is an ad hoc prescribed heating function. It is intended to account for nonradiative thermal forcing by condensation and rainout of tropospheric water vapor as well as other process such as sensible heat transfer from the surface. The effects of changing the distribution and strength of this prescribed heating will be a particular focus of this study. We will use the basic distribution shown in Figure 1 for the prescribed tropospheric heat source or "latent heating." A similar approach to modeling the nonradiative heating of the troposphere is used in other 2-D models [e.g., *Garcia et al.*, 1992].

Our prescribed tropospheric heating in Figure 1a is a simple analytical function of latitude and height described by

$$\mathcal{H}_{latent}(\phi, z, t) = \mathcal{H}_0 \left[F_1(\phi, z, t) + F_2(\phi, z)\right] \quad (4a)$$

where

$$F_1(\phi, z, t) = \mathrm{MAX}\left[1 - \left(\frac{\phi - \phi_{trop}(t)}{\Delta\phi_{trop}}\right)^2 \left(\frac{z}{d_{trop}}\right)^2, \; 0\right] \quad (4b)$$

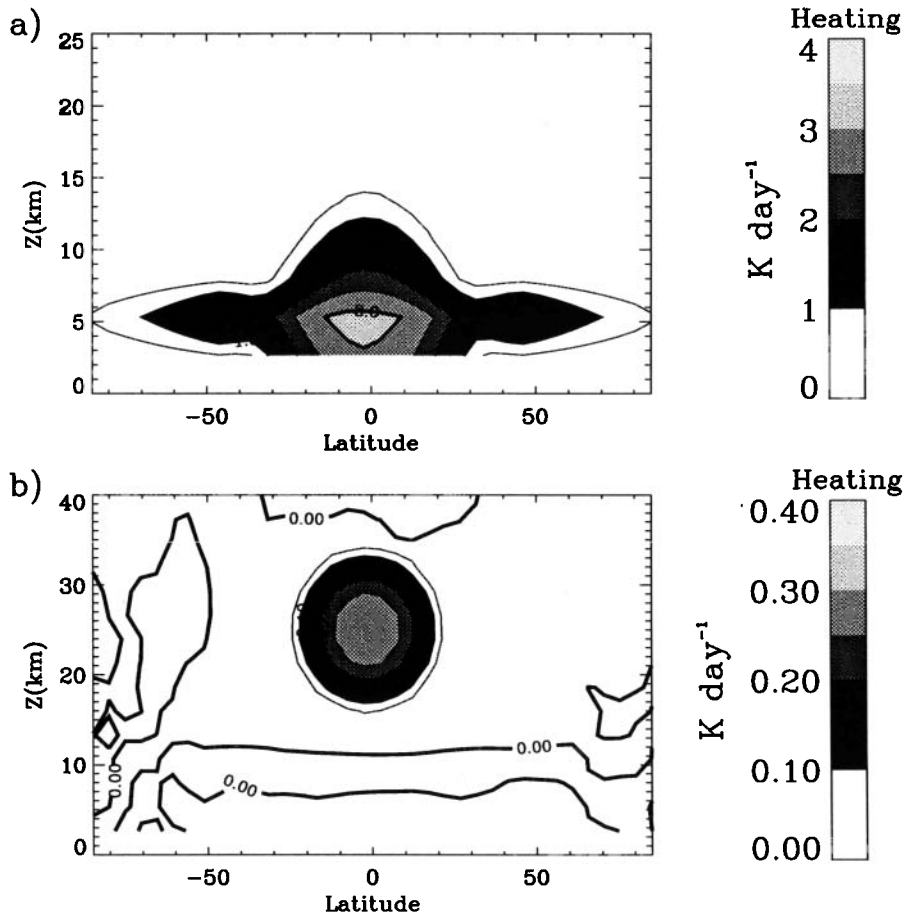

Figure 1. (a) Tropospheric heat source or "latent heating" as a function of latitude and height in October. Heating is shown for $\mathcal{H}_0$=3 K d^{-1}, the value used in most of the experiments discussed. In experiments 5 and 6, $\mathcal{H}_0$ is varied, but the heating distribution in Figure 1a is unchanged except for proportional changes in strength. (b) Additional stratospheric heat source which is used in experiment 7.

and,

$$F_2(\phi, z) = g(z) \exp\left(-\left|\frac{|\phi| - \phi_{\text{mid}}}{\Delta\phi_{\text{mid}}}\right|\right) \qquad (4c)$$

Thus, The function in (4a) is the sum of a deep, broad tropical heat source, represented by F_1, and a shallower midlatitude source, represented by F_2. The width of the tropical source in degrees latitude is given by $\Delta\phi_{\text{trop}}$. We fix $\Delta\phi_{\text{trop}}$ to 35° for all the calculations discussed here. The center of the tropical heating is given by $\phi_{\text{trop}}(t)$, which oscillates between 10°S on June 21 and 10°N on December 21. The horizontal scale of the midlatitude heat source $\Delta\phi_{\text{mid}}$ is set to 30°. The center ϕ_{mid} is fixed at 45° in both hemispheres for the entire year. The vertical distribution of midlatitude heating is given by $g(z)$, which we take to be a sharply peaked function with a maximum value of 1 at 5 km and linear fall off to zero within 2.5 km on both sides of the peak. The depth of the tropical heat source is given by d_{trop} and is set to 15 km for all of experiments in this study. The strength of the heat source $\mathcal{H}_0$ will vary within the range 2.0 K d^{-1} to 4.0 K d^{-1} (Table 2). The motivation for the prescribed heating distribution in Figure 1 comes from inferred climatologies of atmospheric latent heating [e.g., *Newell et al.*, 1970]. These studies show a deep tropical source of latent heat as well as shallow "wings" in midlatitudes. Typical maximum values of latent heating from these climatologies lie between 2.5 K d^{-1} and 3.5 K d^{-1}. Characteristic depths for tropical latent heating are around 15 km.

2.2.3. Lower stratospheric tropical heating. The term $\mathcal{H}_{\text{strat}}$ is included to incorporate small geophysical and theoretical uncertainties in the net heating of the tropical lower stratosphere. Geophysical uncertainties include those arising from aerosols [*Kinne et al.*, 1992; *Rosenfield et al.*, 1997], or cloud albedo variations [e.g., *Eluszkiewicz et al.*, 1996]. Theoretical uncertainties in radiation algorithms arise for example from the suite of radiating gases considered [e.g., *Eluszkiewicz et al.*, 1996]. In all of the simulations to be discussed here except for Experiment 7 (Table 2), $\mathcal{H}_{\text{strat}}$ is zero everywhere. For experiment 7 we use

$$\mathcal{H}_{\text{strat}} = 0.3\left[1 - \left(\frac{\phi - \phi_{\text{trop}}(t)}{\Delta\phi_{\text{strat}}}\right)^2 \left(\frac{z - d_{\text{strat}}}{\Delta z_{\text{strat}}}\right)^2\right] \quad \text{K d}^{-1} \qquad (4d)$$

where ϕ_{trop} is as in (4b), $\Delta\phi_{\text{strat}}$ is set to 25°, d_{strat} is

set to 25 km, and $\Delta z_{\rm strat}$ is set to 10 km. $\mathcal{H}_{\rm strat}$=0 is imposed outside of the range $|\phi-\phi_{\rm trop}(t)|<\Delta\phi_{\rm trop}$, and $|z-d_{\rm strat}|<\Delta z_{\rm strat}$. This function is shown in Figure 1b. The peak of $\mathcal{H}_{\rm strat}$ occurs immediately above that of $\mathcal{H}_{\rm latent}$ at all times and thus also oscillates between 10°N and 10°S.

2.2.4. Surface boundary heating and cooling. The term $\alpha_{\rm bdy}(\bar{\theta}-\bar{\theta}_{\rm NCEP})$ prevents the lower troposphere from cooling to excessively cold temperatures at the poles and in winter midlatitudes. It is nonzero only in the lowest vertical level of the model. At this level, the model potential temperature is relaxed to observed potential temperatures derived from a seven year average of National Center for Environmental Prediction/Climate Analysis Center (NCEP/CAC) analyses. This term can be thought of as a crude parameterization of surface heating effects, including poleward transport of heat by the oceans.

2.2.5. Vertical mixing. The last term in (3) represents vertical redistribution of heat by turbulent and molecular diffusion. Turbulent diffusion of heat is a significant contribution to the total thermodynamic forcing in both the tropical troposphere and in the mesosphere. In the mesosphere, high values of $K_{\rm thrm}$ arise from breakdown of gravity waves. In the troposphere we prescribe large values for $K_{\rm thrm}$ in the tropics to coincide approximately with the tropical latent heat source. Peak values of $K_{\rm thrm}$ in the tropical troposphere are taken to be 10^5 cm^2 s^{-1} at ϕ=$\phi_{\rm trop}$ and to fall off quadratically in both height and latitude. The scales for $K_{\rm thrm}$ are 15 km in the vertical and 35° in latitude. These large vertical diffusivitites act on strong vertical gradients of potential temperature and result in significant fluxes of heat. This distribution of $K_{\rm thrm}$ will be fixed for all of the experiments described here.

2.3. Age of Air and Experimental Design

The mean age of air (henceforth denoted by Γ following *Hall and Plumb* [1994]) in our model simulations will be determined by tracking the evolution of a fictitious "age tracer" $\mu(\phi,z,t)$ with a tropospheric source P and no losses anywhere. The tracer evolution equation is straightforward,

$$\frac{\partial\mu}{\partial t}+v^*\frac{\partial\mu}{a\partial\phi}+w^*\frac{\partial\mu}{\partial z} = P+\frac{1}{\cos\phi}\frac{\partial}{\partial\phi}\left[\cos\phi K_{yy}\frac{\partial\mu}{\partial\phi}\right]+\frac{1}{\rho}\frac{\partial}{\partial z}\left[\rho K_{zz}\frac{\partial\mu}{\partial z}\right] \quad (5)$$

As was the case for (1a) and (1b) the numerical advection of the tracer is performed using the scheme of *Prather* [1986]. The μ tracer (age tracer) is initially uniform throughout the atmosphere. Its initial value is set to 100 units. Below 10 km we set P to be a constant, latitudinally uniform source with a strength of 7 units yr^{-1}, and above 10 km we set P=0. The present calculations include a background or "floor" value for the horizontal eddy diffusion K_{yy} of 10^9 cm^2 s^{-1}. Eddy diffusion from planetary wave breaking $K_{\rm PW}$ is used wherever it exceeds the background value; that is, K_{yy}= MAX[(10^9 cm^2 s^{-1}), $K_{\rm PW}$]. The background value for K_{yy} is included to account for horizontal mixing induced by dynamical processes in the atmosphere not included in our wave 1 planetary wave model. These could include higher-order planetary waves, quasi-geostrophic turbulence, or inertiogravity waves [e.g., *Pierce et al.*, 1994]. The vertical mixing coefficient for tracers K_{zz} is set equal to $K_{\rm thrm}$, the vertical eddy diffusivity for heat.

In order to examine the effects of horizontal mixing on model transport we also track the evolution of a related tracer μ^*. This tracer is initialized and forced identically to μ. However, when (5) is used to calculate the evolution of μ^*, we set K_{yy}=0 identically. Vertical mixing is retained in the evolution of μ^*. Thus by comparing μ and μ^* the maximum possible impact of horizontal mixing on tracer evolution in the model can be assessed.

Transport and vertical mixing in the model troposphere prevent the mean tropospheric mixing ratio of μ or μ^* from possessing exactly the behavior specified by our choice of P. We integrate the model for 12 years and perform a linear fit to the equatorial mixing ratio of the age tracers at the model lower boundary. In practice, this low-level mixing ratio is a nearly linear function of time with a slope of around 5.9 units yr^{-1}. The result of the linear fit is then used to calculate the age at a particular time and location according to,

$$\Gamma=\frac{\mu(0,0,t)-\mu(\phi,z,t)}{(\Delta\mu/\Delta t)_{\rm fit}} \quad (6)$$

where μ can be either the horizontally mixed tracer or the unmixed tracer μ^*. Depending on whether μ or μ^* is used in (6) we refer either to a "mixed" age Γ or to an "unmixed" age Γ^* for the model.

The mixed age Γ determined from (6) should be equivalent to age estimated from measurements of long-lived tracers with time-dependent tropospheric sources, while the unmixed age Γ^* should be close to estimates of age based on air-parcel travel times in a 2-D Lagrangian calculation such as that shown by *Rosenlof* [1995]. Some differences between Γ^* and Lagrangian travel times could still arise due to vertical mixing and implicit numerical diffusion that may still affect the evolution of μ^*. However, for most of the stratosphere K_{zz} is small and numerical diffusion in our advection scheme is known to be small [*Prather*, 1986; *Shia et al.*, 1991; *Bacmeister et al.*, 1995]. Therefore, we expect the unmixed age based on μ^* to be reasonably close to the true 2-D Lagrangian travel times that would be obtained using our model's meridional circulation. In a 2-D TEM model, Γ and Γ^* as defined in (6) can be expected to be quite different The magnitude of difference may be related to the width of the age-spectrum discussed by *Hall and Plumb* [1994] and *Hall and Waugh* [1997] since, at least in the tropics, Γ^* and the the time-of-arrival for the peak in the age spectrum (the "modal time" *Hall and Waugh* [1997]) should be similar.

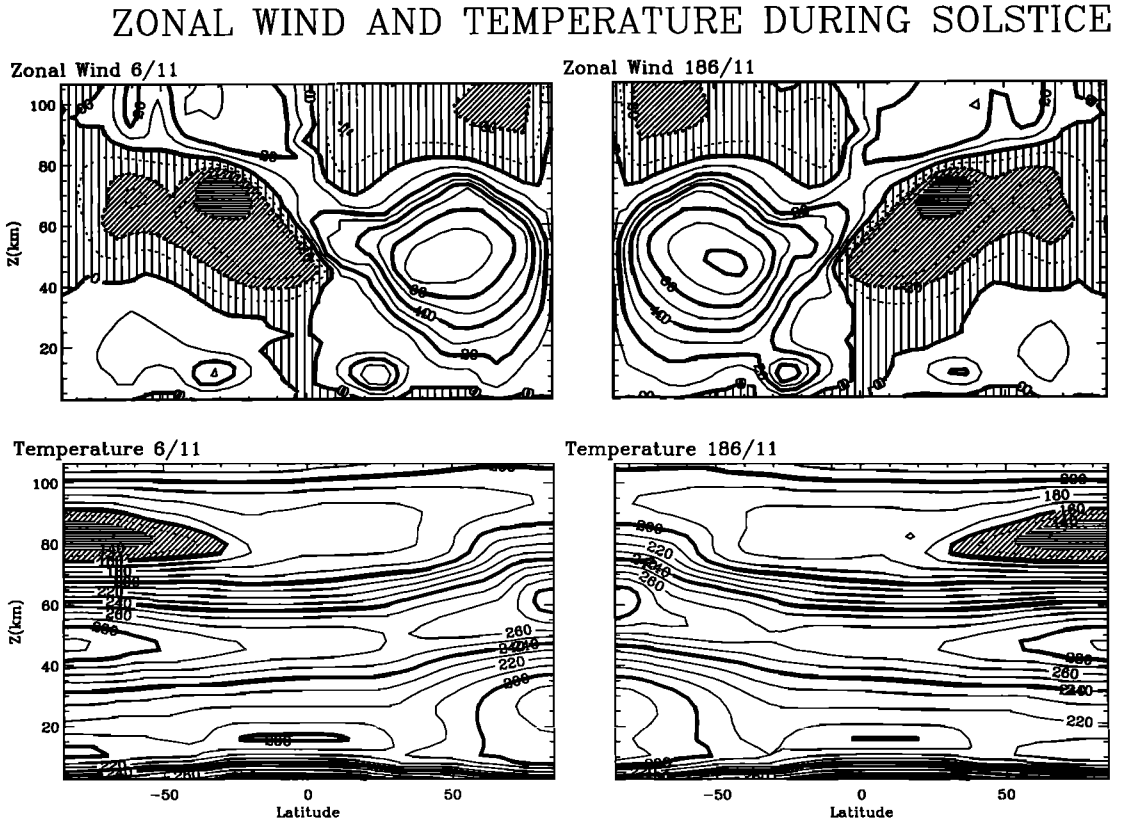

Figure 2. Zonal wind and temperature as a function of latitude and height at both solstices for experiment 1, the baseline simulation. The top panels show model zonal winds; (left) close to northern winter solstice, January 6, and (right) close to summer winter solstice, July 6. Hatching and dashed contours show easterly winds. Thick contours are drawn every 20 m s^{-1}, thin contours every 10 m s^{-1}. The bottom panels show temperatures; (left) near northern winter and (right) near southern winter solstice. Hatching shows temperatures below 160 K. Thick contours are drawn every 40 K, thin contours every 10 K.

3. Results

3.1. Model Climate

Figure 2 shows zonal wind and temperature at solstice conditions for a simulation with peak troposopheric heating $\mathcal{H}_0$=3 K d^{-1} and planetary wave forcing Z_{SH}= 175 m and Z_{NH}= 350 m. As discussed by *Summers et al.* [1997], upper stratospheric and mesospheric zonal wind and temperature fields look reasonable when compared with the climatologies of *Fleming et al.* [1988] and *Randel* [1992]. Minimum summer mesopause temperatures are somewhat lower in the present simulations than in those discussed by Summers et al., T_{min}~120 K compared with T_{min}~140 K. Zonal wind reversals in the upper mesosphere are somewhat more pronounced in the present simulations. These relatively minor changes to the model upper mesosphere are due to differences in the settings for the nonzero phase speed gravity waves shown in Table 1. Summers et al. use a hemispherically asymmetric cubic law drag, which is not done in the present simulations. Here latitudinally uniform cubic law drag is used. This results in somewhat weaker zonal wind and temperature asymmetries above 50 km than were the presented by *Summers et al.* [1997].

In the lower stratosphere and troposphere, larger disagreements between model and observations occur. Subtropical jets in both hemispheres are positioned 5° to 10° too close to the equator compared with NCEP analyses [*Randel*, 1992] and Geophysical Fluid Dynamics Laboratory (GFDL) analyses [*Peixoto and Oort*, 1992]. Observed wintertime subtropical jets in both hemispheres exhibit maximum winds between 30° and 40° latitude, whereas the model jets peak between 20° and 30°. Peak wind speeds in the winter subtropical jets are observed to be near 35 m s^{-1}. One of the worst aspects of the model simulations is an excessively cold midlatitude and polar tropopause. Wintertime extratropical tropopause temperatures in the model are 10 to 20 K too cold, while summertime tropopause temperatures are 20 to 30 K too cold. It is worth noting that in simulations without planetary wave drag, wintertime tropopause temperatures are even 10 K colder than in Figure 2. This suggests that our large errors in polar and midlatitude tropopause temperatures may be due

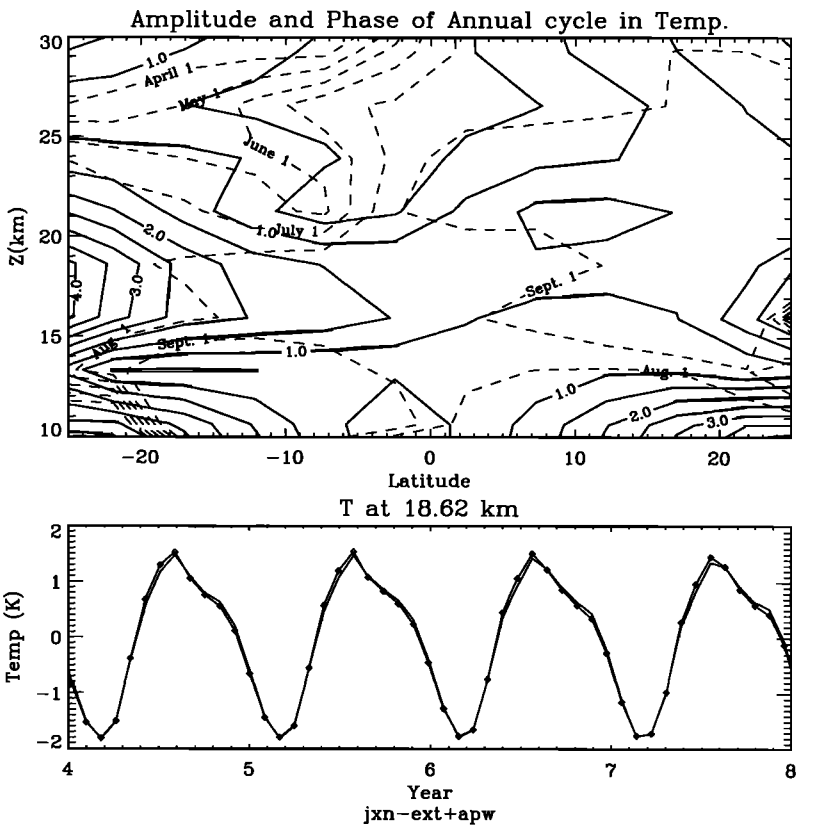

Figure 3. (top) Amplitude (solid contours) and phase (dashed contours) of annual cycle in temperature as a function of latitude and height for experiment 1. Peak-to-peak amplitudes are twice what is displayed. (bottom) Time series of model temperature oscillation at 18 km at 2.5°S and 2.5°N. Annual average has been subtracted.

in part to the omission of heat transport, or forced descent, by baroclinic eddies or other dissipating waves in the troposphere and lower stratosphere. Transport of angular momentum by baroclinic eddies may also move the subtropical jets poleward

3.1.1. Tropical tropopause temperatures

While the model simulation of extratropical tropopause temperatures is somewhat deficient, the simulation of tropical tropopause temperatures is quite good. Values vary annually between 196 K and 200 K, in reasonable agreement with observed tropical tropopause temperatures. Figure 3 shows amplitude and phase for the annual component of temperature variability as a function of latitude and height for the present experiment. Model tropopause temperatures in the tropics exhibit an annual cycle, with minimum values during northern hemisphere (NH) winter and maximum values in southern hemisphere (SH) winter. Figure 3 shows the Fourier amplitude of the annual cycle in the model temperatures, so that peak to peak variations are twice the value displayed. The amplitude of the Fourier analyzed annual cycle is somewhat weak, 2 to 3 K peak to peak, compared the observed 4 to 10 K range reported by numerous investigators [e.g., *Rosenlof and Holton,* 1993; *Yulaeva et al.,* 1994]. However, an examination of the model temperature time history at the tropical tropopause (Figure 3, bottom) shows that the total difference between minimum and maximum tropical tropopause temperatures is close to 4 K.

The phase of the model's annual cycle of temperature at the tropical tropopause is in excellent agreement with observations cited by Yulaeva et al. with temperatures peaking between August 1 and September 1 at 18 km. However, at lower altitudes the observed phase varies rapidly with observed tropical temperatures peaking between February 1 and March 1 below 15 km. In contrast, the phase of our model annual cycle remains relatively constant below 15 km. This disagreement may reflect our model's incomplete simulation of tropospheric processes.

Above 20 km the model's annual cycle in tropical tropopause temperatures decreases rapidly. This is consistent with observations [e.g., *Yulaeva et al.,* 1994; *Garcia et al.,* 1997]. By 30 km, variability in model tropical temperatures is dominated by a semiannual oscillation (SAO). This is also in accord with observations of tropical temperatures [e.g., *Garcia et al.,* 1997]. Our model's SAO is discussed in greater detail by *Summers et al.* [1997].

3.2. Basic Distribution of Γ and Γ^*

We now describe the model distribution of Γ and Γ^* in the baseline simulation. A latitude-height section of Γ after 10.5 years of model integration is shown in Fig-

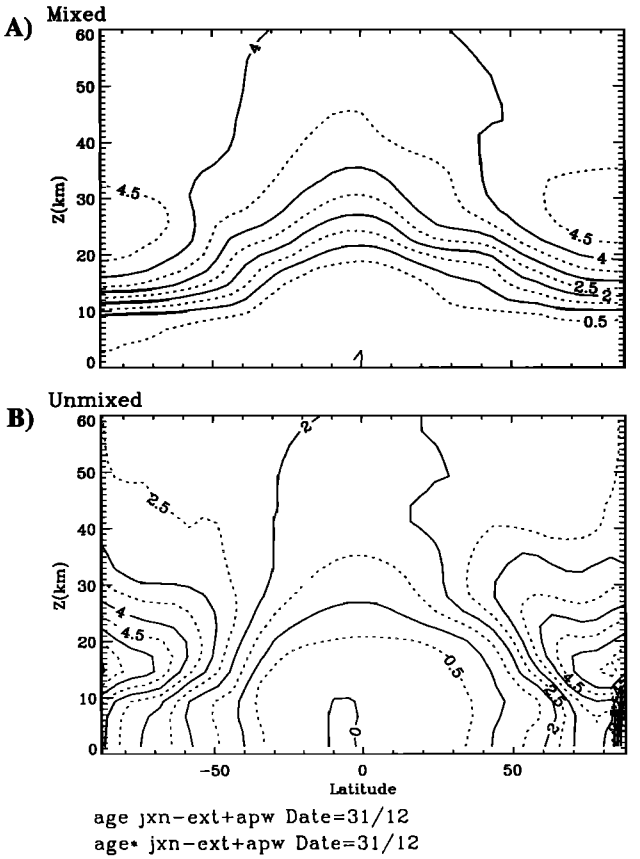

Figure 4. Age of air as a function of latitude and height on day 31 of model year 12 (after 11.5 year integration). (a) Mixed age Γ, (b) unmixed age Γ^* .

ure 4a. The corresponding unmixed age Γ^* is shown in Figure 4b. We show the distribution on day 31 of model year 11, i.e. northern hemisphere winter. Both Γ and Γ^* have a characteristic distribution determined largely by the Brewer-Dobson (residual mean meridional) circulation of the atmosphere. In the model troposphere, prescribed rapid vertical mixing as well as strong vertical motion in the tropics maintain low Γ values (< 1 year). However, significant latitudinal gradients in Γ^* develop throughout the troposphere. Higher values of Γ^* are found near the poles, probably as a result of continual injection from above by annual mean descent over the poles. Nevertheless, in the tropical troposphere both Γ and Γ^* have values below 1 year.

In the tropical stratosphere between 15 and 40 km a strong vertical gradient is present in both mixed and unmixed ages. This gradient is present primarily because of the weak mean vertical and meridional motion in this part of the atmosphere. Comparing Γ (Figure 4a) with Γ^* (Figure 4b), horizontal mixing actually intensifies this vertical gradient. This is most easily interpreted as a simple consequence of exchanging descending parcels with low values of μ from the polar and midlatitude lower stratosphere with ascending tropical air parcels containing higher values of μ. This exchange leads to net aging of the tropical stratosphere and all of the mesosphere, compared to the age which would be present in the absence of horizontal mixing. The only part of the atmosphere where mixing leads to reduced age is the extratropical lower stratosphere. Above 40 km, strong, annually varying meridional winds in the tropics along with strong vertical winds at the poles rapidly distort and homogenize both the μ and the μ^* tracer. This leads to a relatively uniform age-of-air distribution everywhere above 40 km. The mixed age above 40 km is between 3.5 and 4.5 years, while the unmixed age is between 2.0 and 2.5 years.

Thus the basic distribution of Γ in Figure 4, and to a lesser degree Γ^*, consists of two relatively uniform regions, one in the troposphere and another above the midstratosphere. These two regions are divided by a strong vertical gradient in age in the lower stratosphere, which is intensified by horizontal mixing. Further effects of planetary wave mixing are evident in the steplike structure of the contours of Γ in the lower stratosphere. Going south from 90°N at around 20 km, the Γ contours are at first relatively flat with a value around 4 years. Between 45° and 55°N a relatively sharp drop in Γ to values less than 3 years is encountered. From 45° to around 20°N Γ is relatively flat varying between 2.5 to 2 years. Between 15° and 20°N the tropical upward bulge in the age contours begins. At the equator, ages of 1 year or less are found up to 25 km. The location of the well mixed region between 15° and 45°N corresponds roughly to the location of the midlatitude surf zone, which is bounded by the polar vortex edge and subtropical barrier. The edge of the subtropical barrier is somewhat too close to the equator, an error which is probably related to incorrect position of the subtropical jets (Figure 2).

The general features of the lower-stratospheric age distribution shown in Figure 4a are in good agreement with SF_6 measurements taken from the ER-2 [*Elkins et al.*, 1996]. However, values of Γ at 35 km at midlatitudes are low compared to age estimates based on balloon-borne CO_2 measurements taken between 1976 and 1990 [*Schmidt and Khedim*, 1991] as well as recent balloon-borne SF_6 measurements [*Harnisch et al.*, 1996]. The CO_2 measurements give values of age in the midlatitude midstratosphere that vary between 2 and 7 years with a mean of 5.6 years, with the more recent CO_2 measurements suggesting a somewhat lower mean. The SF_6 measurements of Harnisch et al. yield very high ages at midlatitudes, in some cases exceeding 8 years. Our baseline Γ is also somewhat lower than recently published estimates of age based on HALOE HF measurements [*Russell et al.* 1996]. Russell et al. report ages 5.9±2 years at 50 km, so our model result of ~4.0 years is low but still within Russell et al.'s estimated errors.

The unmixed age Γ^* is not an observable quantity. However, Γ^* in Figure 4b is in rough agreement with the age shown by *Rosenlof* [1995, Figure 17] except in the polar lower stratosphere below 20 km where our maximum Γ^* of 5 years is 1.0 to 1.5 years greater than that obtained by Rosenlof. However, above 25 km and in the tropical lower stratosphere our Γ^* is in good agreement with the results of Rosenlof. The age shown by Rosenlof

is based on travel times of Lagrangian air parcels advected by a residual circulation inferred from UKMO analyses of temperature for 1992 and 1993. It is of interest that the model again fails most visibly in the polar lower stratosphere. Both our cold bias and excessively high unmixed age are consistent with insufficient dynamically forced descent in the lowest part of the polar stratosphere. In general though, the similarity between model Γ^* and Rosenlof's Lagrangian age calculations is an encouraging sign that the model meridional circulation is in reasonable agreement with that inferred from atmospheric observations.

3.3. Sensitivity to Planetary Wave Forcing

Planetary wave forcing can affect the model age distribution in two ways. Planetary wave mixing increases the fraction of older midlatitude air which enters the tropical ascent zone of the model. This will tend to increase the age of the middle atmosphere. However, increased planetary wave momentum forcing can also strengthen the meridional circulation, leading to more rapid tropical ascent and a younger middle atmosphere. Unfortunately, the planetary wave forcing in this model can only be incompletely specified from atmospheric observations. Estimates of amplitudes and drag, or EP-flux divergence, for stationary planetary wave 1 have been made from data [e.g, *Randel,* 1992]. These estimates are useful as checks against grossly unrealistic planetary wave amplitudes. However, they are not necessarily useful in choosing parameter settings that yield good simulations of zonally averaged winds and temperatures. For example in the southern winter stratosphere, stationary wave 1 is observed to have geopotential amplitude near 240 m, which is far below 50% of the northern hemisphere observed amplitude of over 960 m [*Randel,* 1992]. Nevertheless, we obtain reasonable simulations using $Z_{SH}=0.5Z_{NH}$. If we forced the planetary wave model with something like the observed ratio of southern to northern hemispheric wave 1 amplitudes (~1:4), our simulation in one of the two hemsipheres would suffer. We speculate that this is because the total planetary wave effect in both hemispheres includes higher wavenumber waves and nonstationary waves which do not possess so large a north-south asymmetry as stationary wave 1. Our model currently simulates only planetary wave 1 forced by orography. The effects of this single wave are expected to account for those of a complete spectrum of stationary as well as transient planetary waves. It is therefore of great interest to examine the sensitivity of our simulations to the choice of planetary wave forcing amplitudes Z_{SH} and Z_{NH}. In order to restrict parameter space and to simplify interpretation of the results in this Section, we limit our attention to experiments with symmetric planetary wave forcing; that is, $Z_{SH}=Z_{NH}\equiv Z_{NSH}$.

Figure 5 shows the final distributions of Γ for experiments with Z_{NSH}=125, 250, and 350 m (experiments 2-4, Table 2). The final Γ for experiment 2 with Z_{NSH}=250 m (Figure 5a) is very similar to that for experiment 1, with an average Γ in the middle atmosphere

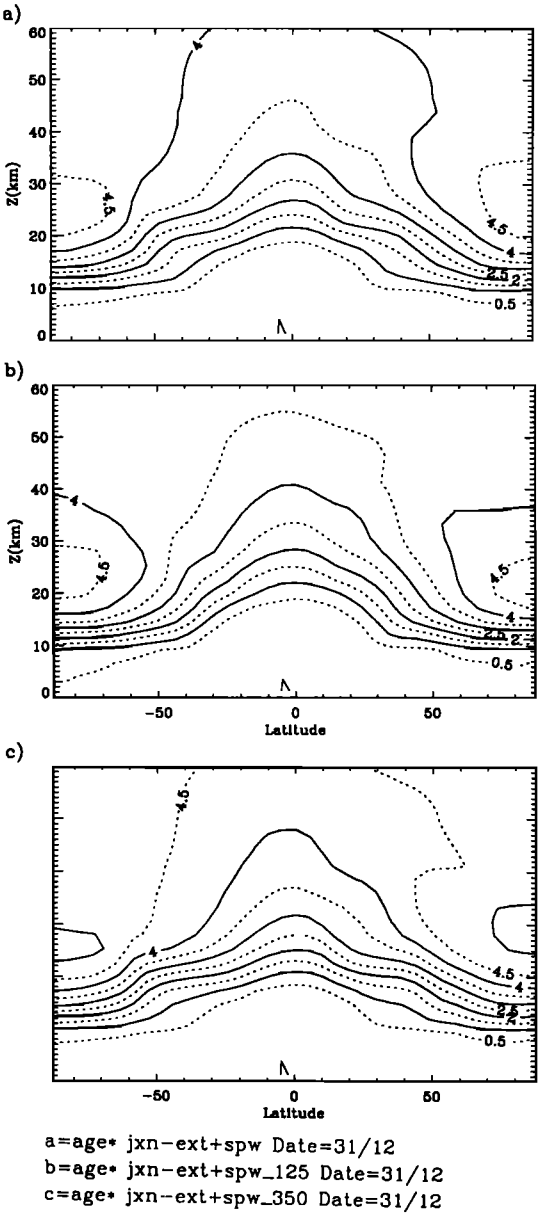

Figure 5. Γ as a function of latitude and height on day 31 of model year 12 for experiments with fixed tropospheric heating and varying symmetric planetary wave forcing amplitudes. (a) Z_{NSH}=250 (experiment 2). (b) Z_{NSH}=125 (experiment 3). (c) Z_{NSH}=350 (experiment 4).

close to 4 years in both experiments. Generally speaking, the broad features of the distribution of Γ are similar in all of the experiments. However, Γ in the stratosphere and mesosphere shows a systematic dependence on the amplitude of planetary wave forcing. Typical values for Γ at 50 km vary from a low value of 3.5 years for experiment 3 with Z_{NSH}=125 m (Figure 5b), to a high value 4.5 years for experiment 4 with Z_{NSH}=350 m (Figure 5c). Thus, there is a systematic decrease in Γ as planetary wave-forcing amplitudes are reduced.

In contrast to the systematic variation of the mixed age Γ, the unmixed stratospheric age Γ^* for experiments

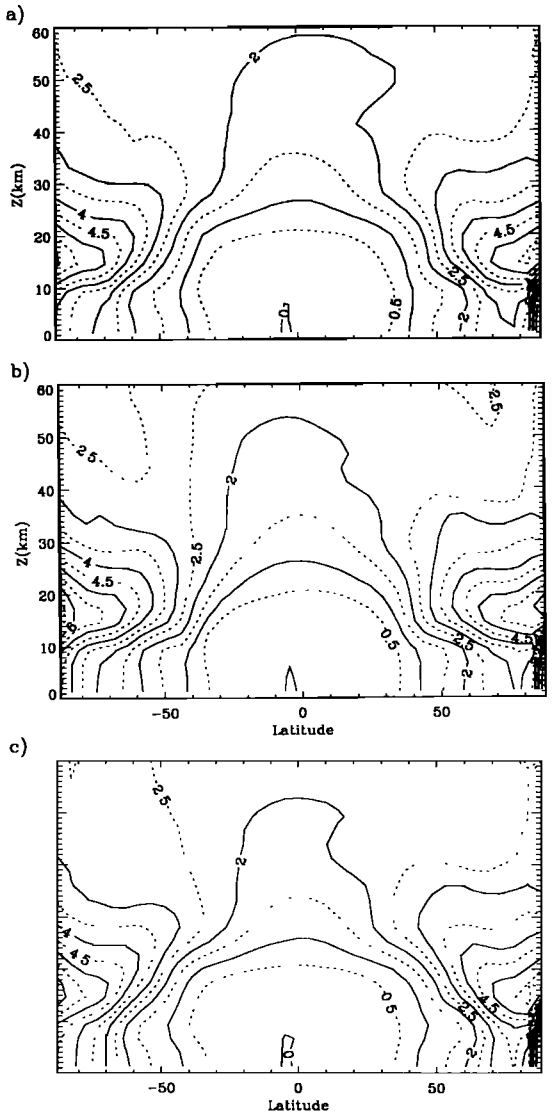

Figure 6. Same as Figure 5 except for Γ^*.

2–4 in Figure 6 reveals little consistent variation with Z_{NSH}. The average value of Γ^* at 50 km is around 2.5 years for all of the experiments. Minor differences occur between experiments, with some hint of reduced upward motion in the tropics for Z_{NSH}=350 m. However, overall, the distribution of unmixed age in all three experiments is nearly the same. This can only be the case if the tropical ascent rates in all three experiments with different Z_{NSH} are similar. Thus the increase in Γ with increasing planetary wave forcing must be due primarily to enhanced horizontal mixing. Figure 7 shows time-averaged K_{yy} in the lower stratosphere. Zones of strong planetary wave mixing in midlatitudes are clearly evident, and the magnitude of this midlatitude mixing depends strongly on Z_{NSH}. Little if any enhancement of K_{yy} over the background value of 10^9 cm^2 s^{-1} occurs for experiment 3 (dotted line), whereas maximum K_{yy} values of nearly 10^{10} cm^2 s^{-1} occur for experiment 4. (dashed line). Figure 8 shows profiles of time- and latitude-averaged residual vertical velocity $< \overline{w^*}^t >_{20}$ in the tropics for experiments with varying planetary wave parameters. In the following, $< \overline{(\,)}^t >_\phi$ will be used to indicate a time average over 3 model years and a latitude average about the equator between $+\phi$ and $-\phi$ degrees. Below 18 km, $<\overline{w^*}^t>_{20}$ has a clear dependence on Z_{NSH} with weaker planetary wave forcing giving weaker $<\overline{w^*}^t>_{20}$. However, little effect on $<\overline{w^*}^t>_{20}$ is noticeable between 18 and 40 km, where all of the curves lie close to one another.

The insensitivity of $\overline{w^*}^t$ to increased planetary wave forcing is puzzling, particularly since K_{yy} and EP-flux divergence are directly connected in the model's planetary wave parameterization. Time averaged profiles of $\nabla \cdot \mathbf{F}_{\mathrm{PW}}$ at 30°N are shown in Figure 8. As Z_{NSH} increases, the largest increases in $\overline{\nabla \cdot \mathbf{F}_{\mathrm{PW}}}^t$ are seen below 22 km. This is high enough to create a mixing zone that can interact with tropical ascent. However, the circulation effects of this added drag are directed downward, and thus have little impact on the speed of tropical ascent above 20-25 km. Between 22 and 40 km, $\overline{\nabla \cdot \mathbf{F}_{\mathrm{PW}}}^t$ at 30°N for Z_{NSH}=250 and Z_{NSH}=350, are similar indicating that planetary waves have reached saturation by the time they reach these altitudes. As pointed out by *Garcia* [1991], increased planetary wave forcing may be reflected primarily in the size of the planetary wave breaking region rather than in the strength of the drag in a model with saturation-limited waves.

This pattern of response to changes in planetary wave forcing may be exaggerated by the model's somewhat unrealistic wind distribution in the troposphere. The separation of tropospheric and middle atmospheric jets (Figure 2) may lead to early saturation of planetary waves originating in the troposphere. If this separation were reduced, changes in EP-flux divergence could be distributed over a deeper layer of the atmosphere. However, winter profiles of $\nabla \cdot \mathbf{F}_{\mathrm{PW}}$ from our simulations (Figure 8) agree reasonably well with climatologies for northern hemisphere winter [e.g., *Randel*, 1992] although our maximum winter values in the lower stratosphere are somewhat lower than in Randel, which could lower the sensitivity of $\overline{w^*}^t$ to changes in planetary wave forcing. Nevertheless, the overall wintertime pattern of EP flux in our simulations agree reasonably well with climatology. In section 4 we explicitly calculate the vertical motion forced solely by mechanical drag, and find it to be small compared to that forced by other terms. This suggests that even doubling the EP flux divergence in our simulations would have a limited effect on tropical upwelling.

3.4. Sensitivity to Latent Heating

As discussed in section 2 the term $\mathcal{H}_{\mathrm{latent}}$ is a crude attempt to represent the heating of the atmosphere by irreversible condensation of water vapor. Latent heating is as yet impossible to measure directly, so it must

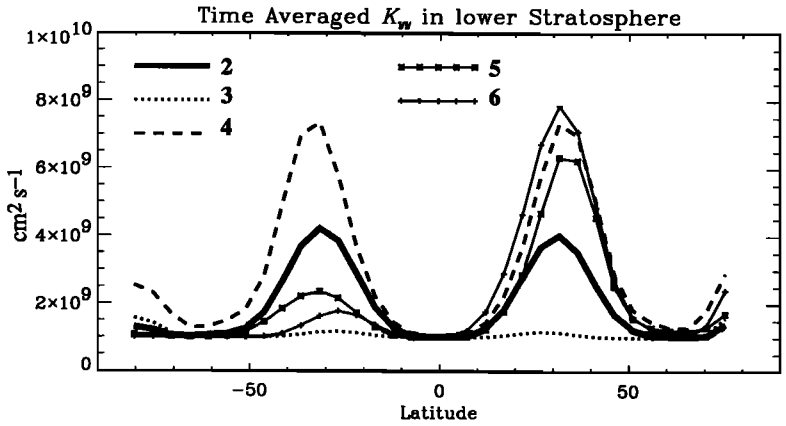

Figure 7. Multiyear average of horizontal eddy-mixing coefficient K_{yy} between 15 and 22 km as a function of latitude for experiments 2-6. Thick solid line shows K_{yy} for experiment 2. Dotted line shows K_{yy} for experiment 3, and dashed line shows curve for experiment 4. Little enhancement over the background value of $10^9 \text{cm}^2\ \text{s}^{-1}$ occurs for experiment 3 where Z_{NSH}=125 m is used. All other experiments show evidence of large midlatitude "surf zones." Thin lines connecting symbols show curves for experiments 5 and 6, i.e., fixed asymmetric planetary wave forcing with varying $\mathcal{H}_0$. Only comparatively small changes in K_{yy} occur as $\mathcal{H}_0$ decreases, with K_{yy} appearing to increase slightly as $\mathcal{H}_0$ decreases.

be inferred as a residual term in a heating budget, or it must be inferred from climatological rainfall rates. Unfortunately, latent heating is the most important contribution to tropospheric diabatic heating [cf. *Peixoto and Oort*, 1992, Figure 13.2]. Clearly, the number of "reasonable" modifications to the distribution shown in Figure 1 is huge. We will therefore limit ourselves to changing the strength of the latent heat source $\mathcal{H}_0$ in (4). We use a low value of $\mathcal{H}_0$=2 K d^{-1} (experiment 5, Table 2) and a high value of $\mathcal{H}_0$=4 K d^{-1} (experiment

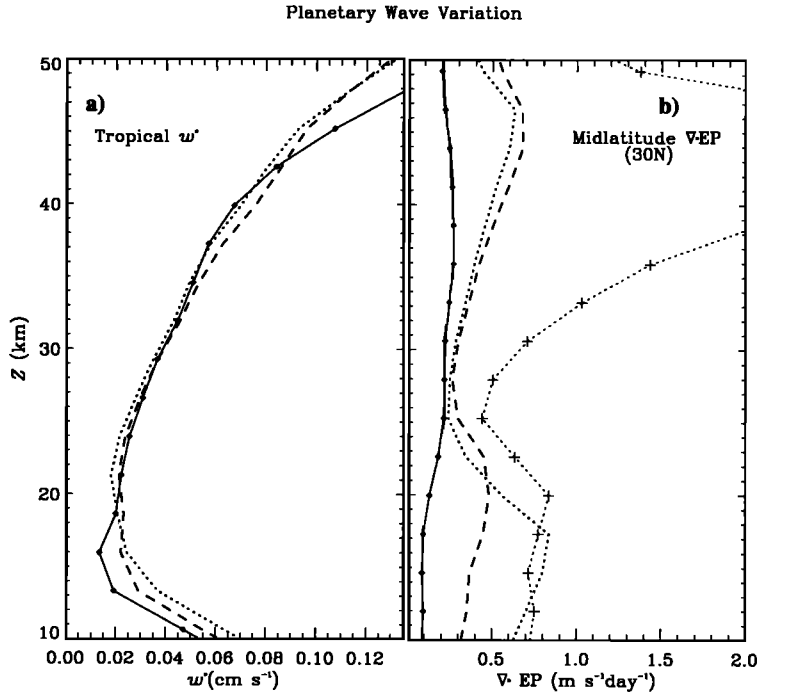

Figure 8. (a) Vertical wind averaged in time over 3 model years and horizontally between 20°S and 20°N $<\overline{w^*}^t>_{20}$ as a function of altitude for experiments with varying planetary wave forcing. Long dashed curve shows $<\overline{w^*}^t>_{20}$ for experiment 2 (Z_{NSH}=250 m). Thin curve connecting diamonds shows $<\overline{w^*}^t>_{20}$ for experiment 3 (Z_{NSH}=125 m). Dotted curve shows result for experiment 4 (Z_{NSH}=350 m). (b) Planetary wave EP-flux divergence at 30°N averaged over 3 years as a function of altitude. Line styles are the same as in Figure 8a. Additional dashed line connecting crosses shows Planetary wave EP-flux divergence for experiment 1 at 30°N on day 16 of model year 3.

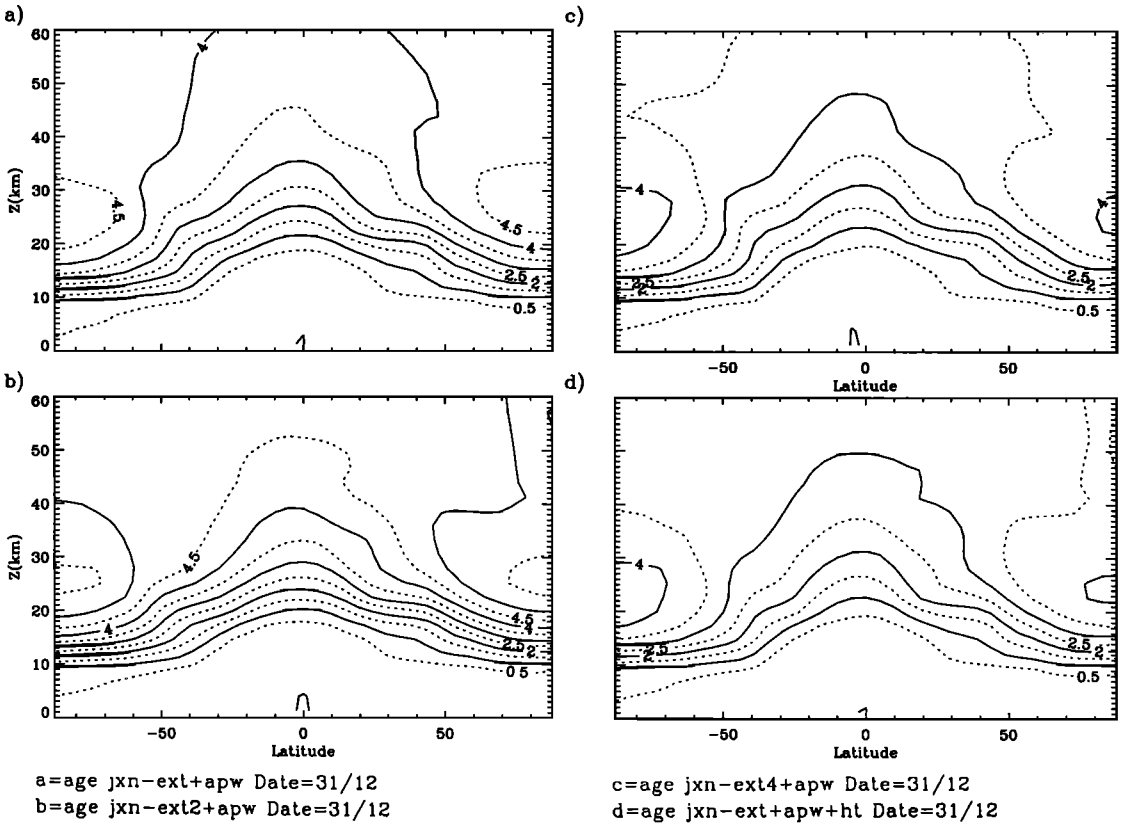

Figure 9. Γ as a function of latitude and height on day 31 of model year 12 for experiments with fixed asymmetric planetary wave forcing amplitudes and varying tropospheric heating. (a) $\mathcal{H}_0$=3 K d^{-1} (experiment 1). (b) $\mathcal{H}_0$=2 K d^{-1} (experiment 5). (c) $\mathcal{H}_0$=4 K d^{-1} (experiment 6). (d) $\mathcal{H}_0$=3 K d^{-1} with additional stratospheric heat source (experiment 7). Note that Figures 4a and 9a are identical.

6, Table 2). Both of these experiments use the same asymmetric planetary wave forcing and inputs to $\mathcal{H}$ as in Experiment 1 (i.e., Z_{NH}=350 m and Z_{SH}=175 m).

Zonal cross sections of Γ at the end of the simulations using different values of $\mathcal{H}_0$ (Experiments 1, 5, and 6) are shown in Figures 9a-9c. A clear and systematic dependence on $\mathcal{H}_0$ is evident. There is a nearly 2 year difference in Γ between the experiment with the youngest middle atmosphere and that with the oldest. In experiment 5 with $\mathcal{H}_0$=2 K d^{-1}, the greater part of the middle atmosphere above 40 km is between 4.5 and 5.0 years old with portions of the polar lower stratosphere approaching 6 years in age (Figure 9a). In a 20 year simulation with $\mathcal{H}_0$=2 K d^{-1}, the oldest air eventually exceeds 6 years in age. This Γ distribution may actually be in better agreement with tracer-based estimates than our "baseline" Γ distribution form experiment 1. In contrast, for experiment 6 with $\mathcal{H}_0$=4 K d^{-1} (Figure 9b) the bulk of the model middle atmosphere is less than 3.5 years old. Planetary wave mixing is not responsible for changes in Γ between experiments 5 and 6. The K_{yy} curves for experiments 5 and 6 (Figure 7) lie relatively close to one another, with maximum NH values between 6×10^9 and 8×10^9 cm^2 s^{-1}. Given that the large, order-of-magnitude differences in K_{yy} for different Z_{NSH} resulted in only one year differences in Γ, it is unlikely that the small K_{yy} changes for different $\mathcal{H}_0$ are producing the nearly 2 year spread in middle atmospheric age between experiments 5 and 6.

The Γ^* distribution for experiments 1, 5, and 6 are shown in Figures 10a-10c. The unmixed age Γ^* also shows a clear systematic dependence on $\mathcal{H}_0$. As $\mathcal{H}_0$ increases from 2 K d^{-1} to 4 K d^{-1}, the average unmixed age at 50 km decreases from around 2.7 years (Figure 10b) to somewhat less than 2.0 years (Figure 10c). This reduction in Γ^* with increasing $\mathcal{H}_0$ is the result of increased w^* in the tropical lower stratosphere, as can be seen in Figure 11. Thus varying the imposed tropical tropospheric heating has a substantial effect on tropical ascent in our model, whereas varying the planetary wave forcing at midlatitudes did not. It is worth noting that while the unmixed age Γ^* changes significantly as $\mathcal{H}_0$ varies, the changes in Γ^* are at most half as large as the changes seen in the mixed age Γ. Thus a simple increase in the time required to advect a parcel of air into the middle atmosphere does not explain the total increase in Γ as $\mathcal{H}_0$ decreases. It appears that horizontal mixing amplifies the delay in vertical transport as the residual mean vertical velocity decreases, even though the mixing coefficient itself showed only a weak dependence on $\mathcal{H}_0$.

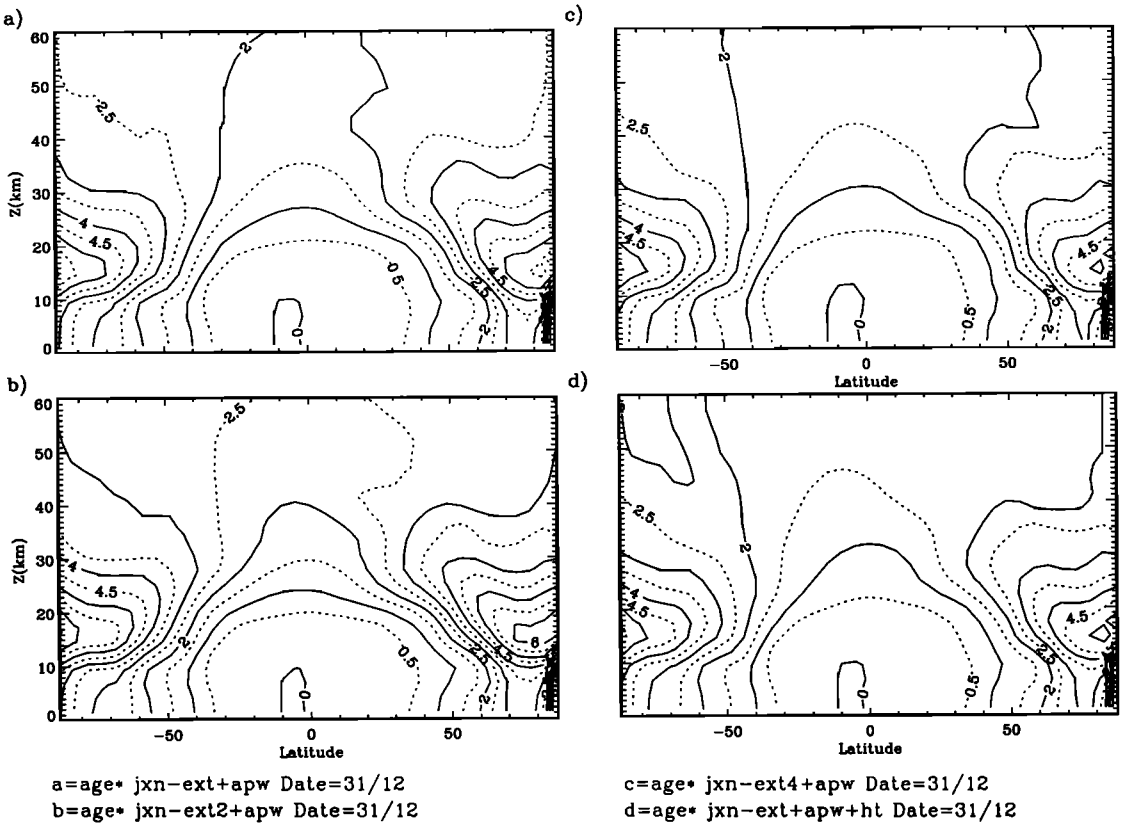

Figure 10. Same as Figure 9 except for Γ^*. Note Figures 4b and 10a are identical.

4. Vertical Motion in the Tropics

4.1. Comparison With HALOE Water Vapor in the Tropics

Figure 11 shows that the model's vertical velocity in the tropical stratosphere is sensitive to the choice of prescribed tropospheric heating. Unfortunately, direct measurements of the residual mean vertical motion are not available for comparison. However, recent satellite observations of water vapor have given what may be an indirect observation of the residual mean vertical motion in the tropical lower stratosphere. The mixing ratio of water vapor entering the stratosphere in the tropics is modulated by the annual cycle in tropical tropopause temperatures with cold tropopause temperatures leading to drier stratospheric air [*Newell and Gould-Stewart*, 1981; *Mote et al.*, 1995]. Minimum tropical tropopause temperatures during northern winter (< 197 K) result in water vapor mixing ratios of 3.5 ppmv. Water vapor mixing ratios rise to near 4.5 ppmv during northern summer as tropopause temperatures climb over 201 K. This annually varying signal in water vapor mixing ratio rises through the tropical lower stratosphere, preserving its identity for over a year and a half [*Mote et al.*, 1995, 1996]. This feature of the tropical stratosphere has been recently dubbed the "atmospheric tape recorder."

Hall and Waugh [1997] have used model age spectra to argue that in the tropical stratosphere an annually varying signal like that of water vapor will rise with a speed described by the "modal time" of the age spectrum rather than its first moment Γ. The modal time (τ_M in the work of *Hall and Waugh* 1997) represents the time taken by the greatest fraction of mass to reach a certain point, i.e., the peak of the age spectrum. The success of Lagrangian parcel calculations in reproducing the motion of water vapor minima and maxima [e.g.,*Mote et al.*, 1996] indicates that τ_M approximates the Lagrangian travel time of an air parcel, at least in the tropical lower stratosphere. In other words, in the tropics we should have $\tau_M \approx \Gamma^*$, and we therefore expect the vertical motion of the unmixed age tracer μ^* to compare well with tropical water vapor observations.

Plates 1a-1c show the evolution of latitude-averaged unmixed age tracer $<\mu^*>_{12}$ as a function of height and time for the experiments with varying $\mathcal{H}_0$ (experiments 1, 5, and 6). Below 18 km the tracers are rapidly mixed and/or advected vertically so that little or no vertical gradient is evident in the isopleths of $<\mu^*>_{12}$. Between 18 km and about 35 km, a region of slow upward drift exists. In this layer the sensitivity of vertical motion to $\mathcal{H}_0$ is clearly evident. By 35 km the isopleths of $<\mu^*>_{12}$ from Experiment 6 with $\mathcal{H}_0$=4 K d^{-1} (Plate 1c) are about 0.75 years ahead of those from Experiment 5 with $\mathcal{H}_0$=2 K d^{-1} (Plate 1a). Above 35 km the isopleths from the different experiments again become steeper and nearly parallel, reflecting the increasingly vigorous meridional circulation at these altitudes. Thus, most of the difference in unmixed age of air between experiments develops in the slow ascent region between 18 and 35 km. The same is true for mixed

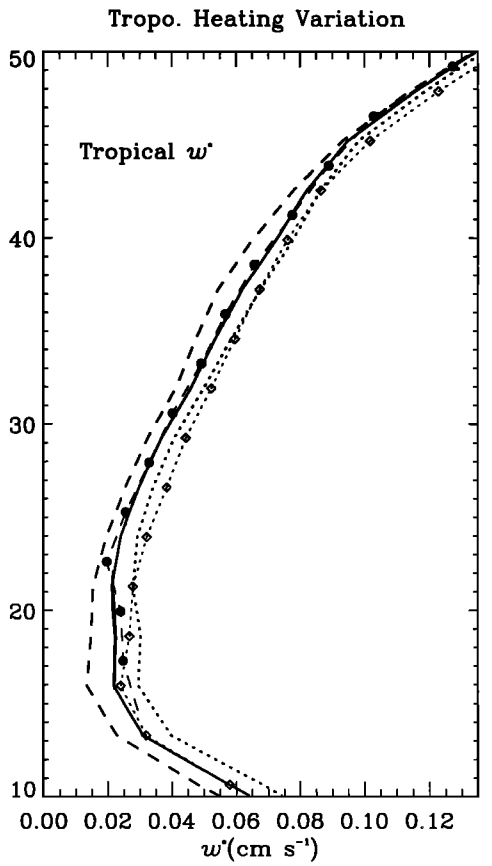

Figure 11. Vertical wind averaged in time over several model years and horizontally between 20°S and 20°N ($<\overline{w^*}^t>_{20}$) as a function of altitude for experiments with varying tropospheric heating. Solid curve shows $<\overline{w^*}^t>_{20}$ for experiment 1 ($\mathcal{H}_0$=3 K d^{-1}). Long-dashed curve shows $<\overline{w^*}^t>_{20}$ for experiment 5 ($\mathcal{H}_0$=2 K d^{-1}). Dotted curve shows $<\overline{w^*}^t>_{20}$ for experiment 6 ($\mathcal{H}_0$=4 K d^{-1}). Thin-dashed lines connecting open diamonds show $<\overline{w^*}^t>_{20}$ for experiment 7 ($\mathcal{H}_0$=3 K d^{-1} with $\mathcal{H}_{strat}$). Note that $<\overline{w^*}^t>_{20}$ for experiments 1 and 7 converge below 15 km. Dashed line joining solid circles shows a profile of $<\overline{\mathcal{H}/\Theta_z}^t>_{20}$, an approximation to the steady state vertical velocity, for experiment 1.

age, which shows a qualititavely similar time evolution in the tropics, except that the isopleths of mixed age rise more slowly.

The color background for Plates 1a-1c shows HALOE 2(CH_4)+H_2O mixing ratio data from the tropics averaged between 8.5°S and 8.5°N as a function of height and time. Similar figures based on MLS as well as HALOE H_2O measurements have been shown elsewhere [e.g., *Mote et al.*, 1995, 1996]. We show them in Plate 1 simply to facilitate comparison with the present model results. The overall pattern of time evolution of the model $<\mu^*>_{12}$ is very similar to that of the HALOE data. The HALOE data in Plate 1 exhibit a layer of slow ascent between 18 and 30 km. This is evident in the shallow slope of minima and maxima of water vapor or 2(CH_4)+H_2O in time-height plane. Above 30 km the "tape recorder" signal weakens quickly, but it appears that ascent is becoming more rapid. Below 20 km the data also suggest more rapid vertical transport (this is clearer in Plates 1a and 1b of *Mote et al.* [1996]). The traces of the water vapor minima and maxima in the HALOE data imply a typical transit time of about 1.0 year between 20 km and 30 km, although there is significant interannual variability. Note the relatively rapid ascent between July 1993 and April 1994 and the relatively slow ascent commencing in July 1995. Overall, there is good quantitative agreement between $<\mu^*>_{12}$ in experiments 1 and 5 in the 18 to 35 km layer and HALOE 2(CH_4)+H_2O, while ascent in experiment 6 ($\mathcal{H}_0$=4 K d^{-1}) is somewhat too rapid.

4.2. Forcing of Model Vertical Motion in the Tropics

The sensitivity of w^* and Γ to prescribed tropospheric heating shows that poorly or incompletely simulated tropospheric processes in a 2-D zonally averaged model can have an impact well into the middle atmosphere. Identifying the ultimate forcing for vertical motion in the tropical stratosphere in a nonlinear 2-D model is complicated by the fact that both drag and heating produce nonlocal circulations, which then lead to nonlocal changes in temperature and zonal wind. Changes in zonal wind or temperature can of course lead to further changes in drag and heating and so on. Remote forcing by midlatitude drag is currently believed to be the most important forcing for vertical motion in the tropical lower stratosphere [e.g., *Iwasaki*, 1992; *Yulaeva et al.*, 1994; *Holton et al.*, 1995]. However, in this section we will show that the sensitivity of our age simulations to tropical heating occurs without a significant contribution from midlatitude planetary wave drag. First, we examine in more detail the time behavior of w^* and components (see below) of w^* in the tropical stratosphere during the age simulations in section 3. Then we will examine the changes to the stream function as $\mathcal{H}_0$ varies.

4.2.1. Decomposition of the residual circulation. . The residual circulation in the quasigeostrophic TEM formulation is obtained from a linear elliptic equation forced by gradients of the momentum forcing X (2) and total heating $\mathcal{H}$ (3), [e.g., *Andrews et al.* 1987, Equation 3.5.7]. The total residual circulation can thus be broken down into a sum of separate circulations forced by the individual terms, or groups of terms, in X and $\mathcal{H}$. Each of these component circulations is that which would result if no additional atmospheric response occurred as a result of the particular component circulation under consideration (e.g., the adiabatic responses to momentum forcing shown by *Haynes et al.* [1991] and by *Holton et al.* [1995, Figure 4a]. The Appendix analyzes the development of "downward control" [*Haynes et al.*, 1991] in terms of such component stream functions.

4.2.2. Seasonal variation of vertical velocity in the tropics . Figure 12 shows model time series

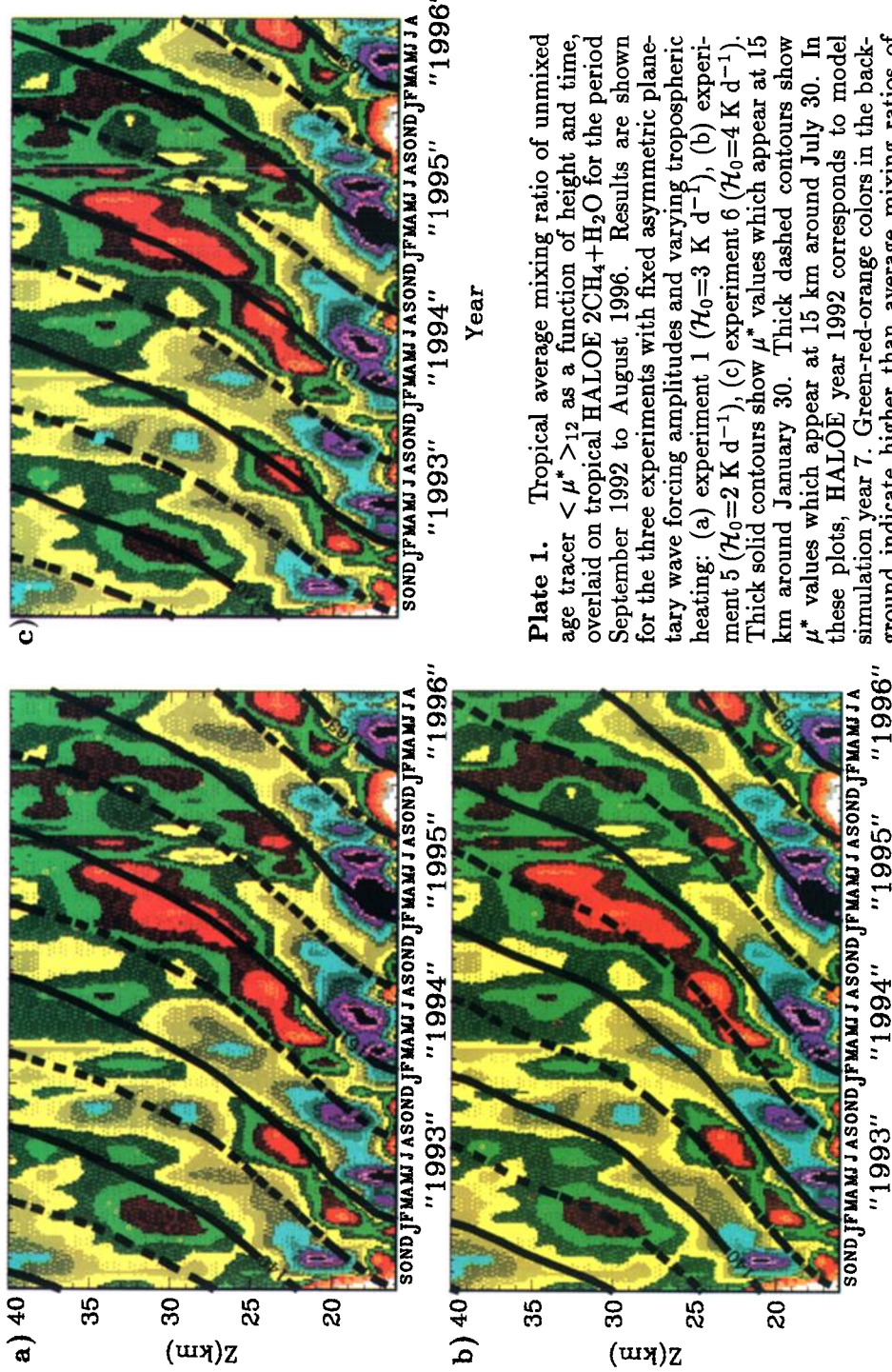

Plate 1. Tropical average mixing ratio of unmixed age tracer $<\mu^*>_{12}$ as a function of height and time, overlaid on tropical HALOE $2CH_4+H_2O$ for the period September 1992 to August 1996. Results are shown for the three experiments with fixed asymmetric planetary wave forcing amplitudes and varying tropospheric heating: (a) experiment 1 ($\mathcal{H}_0$=3 K d^{-1}), (b) experiment 5 ($\mathcal{H}_0$=2 K d^{-1}), (c) experiment 6 ($\mathcal{H}_0$=4 K d^{-1}). Thick solid contours show μ^* values which appear at 15 km around January 30. Thick dashed contours show μ^* values which appear at 15 km around July 30. In these plots, HALOE year 1992 corresponds to model simulation year 7. Green-red-orange colors in the background indicate higher than average mixing ratios of HALOE $2CH_4+H_2O$, i.e., from around 7.1 ppm (green) to 7.5 ppm (orange). Yellow colors indicate mixing ratios going from around 6.2 to 7.0 ppm. Black-purple-blue shades indicate lower than average mixing ratios, going from below 5.6 ppm (black) to around 6.0 ppm (blue). (HALOE $2CH_4+H_2O$ image courtesy of P. A. Newman, NASA Goddard Space Flight Center, Greenbelt, Maryland).

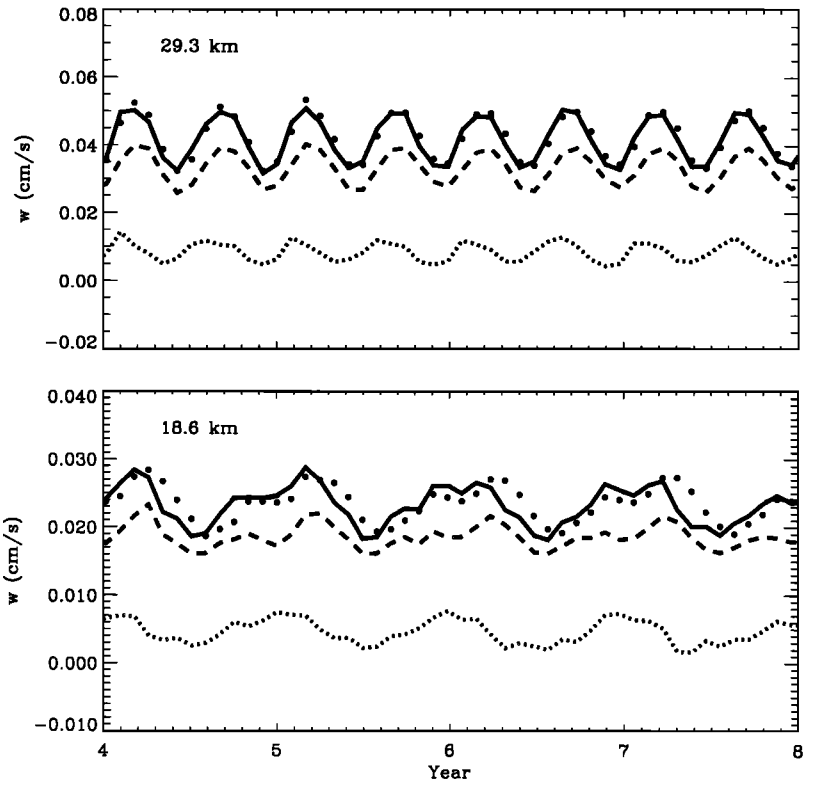

Figure 12. Time series of various components of tropically averaged residual vertical velocity $< w^* >_{20}$ at 18 km (bottom) and 29 km (top) for experiment 1. The solid curves show the total vertical velocity $< w^* >_{20}$. Short-dashed curves show the drag induced component $< w^*_{\mathcal{X}} >_{20}$, and long-dashed curves show the thermally induced component $< w^*_{\mathcal{H}} >_{20}$. Circles show a time-series of $< \mathcal{H}/\overline{\Theta}_z >_{20}$, an approximation to the steady state vertical velocity.

of various components of $< w^* >_{20}$ for experiment 1 at 18 km and 29 km. The vertical velocity has been broken down into two components: $w^*_{\mathcal{X}}$, which is forced by the total drag, and $w^*_{\mathcal{H}}$, which is forced by the total net heating. The sum of these is the total residual vertical velocity w^*. Figure 12 shows that $< w^* >_{20}$ as well as $< w^*_{\mathcal{X}} >_{20}$ and $< w^*_{\mathcal{H}} >_{20}$ have a clear annual cycle at 18 km. The amplitude of the annual cycle in w^* is around 0.005 cm s^{-1}, which yields a roughly estimated heating/cooling rate of 0.05 K d^{-1}, more than sufficient to account for the model's 1–2 K annual cycle at the tropical tropopause. However, in our model this annually varying signal is superimposed on a "floor" value of w^* close to 0.020 cm s^{-1} as indicated in the figure. Thus in our model the amplitude of the annually varying signal in w^* is around one third of this floor value. This means that although significant wave-induced annual variations in tropopause w^* occur in our model, they are superimposed on a relatively large time independent flux through the tropopause. The total amplitude of the annual cycle of tropical w^* at 18 km comes in roughly equal parts from $w^*_{\mathcal{X}}$ and $w^*_{\mathcal{H}}$. However, the "DC" portion of the time series of $< w^* >_{20}$ is almost entirely contributed by $w^*_{\mathcal{H}}$. The phasing of $< w^*_{\mathcal{X}} >_{20}$ and $< w^*_{\mathcal{H}} >_{20}$ is slightly different, with $w^*_{\mathcal{X}}$ peaking around January 1 and $w^*_{\mathcal{H}}$ peaking in March. The presence of an annual cycle in $w^*_{\mathcal{H}}$ is a clear indication that midlatitude drag is indirectly inducing a thermally forced circulation, as discussed in the Appendix. Note also that $< w^*_{\mathcal{H}} >_{20}$ and $< \mathcal{H}/\overline{\Theta}_z >_{20}$ are slightly out of phase, which is another indication of remote forcing.

At 29 km the situation is quite different. Little annual cycle is evident, but a strong semi-annual cycle is visible in all components of $< w^* >_{20}$. The momentum forced circulation $w^*_{\mathcal{X}}$ contributes a smaller fraction to the semiannual cycle in tropical w^* than does $w^*_{\mathcal{H}}$. The phase of $< w^*_{\mathcal{H}} >_{20}$ at 29 km is close to that of $< \mathcal{H}/\overline{\Theta}_z >_{20}$ with maxima occurring near both equinoxes. In contrast, the phase of $< w^*_{\mathcal{X}} >_{20}$ is shifted such that maxima occur somewhat close to the solstices. As was the case at 18 km, the mean value of $< w^* >_{20}$ is substantially larger than the amplitude of the time-varying portion and is contributed primarily by $< w^*_{\mathcal{H}} >_{20}$. The weak annual cycle and strong semiannual cycle in $< w^* >_{20}$ at 29 km is consistent with tropical or hemispherically symmetric forcing rather than with asymmetric midlatitude planetary wave drag. The relationship of our models SAO in zonal wind, which is weak below 30 km [*Summers et al.*, 1997], to the SAO in w^* is not yet clear.

The presence of annual cycle in $< w^* >_{20}$ at 18 km agrees with the idea that vertical motion through the

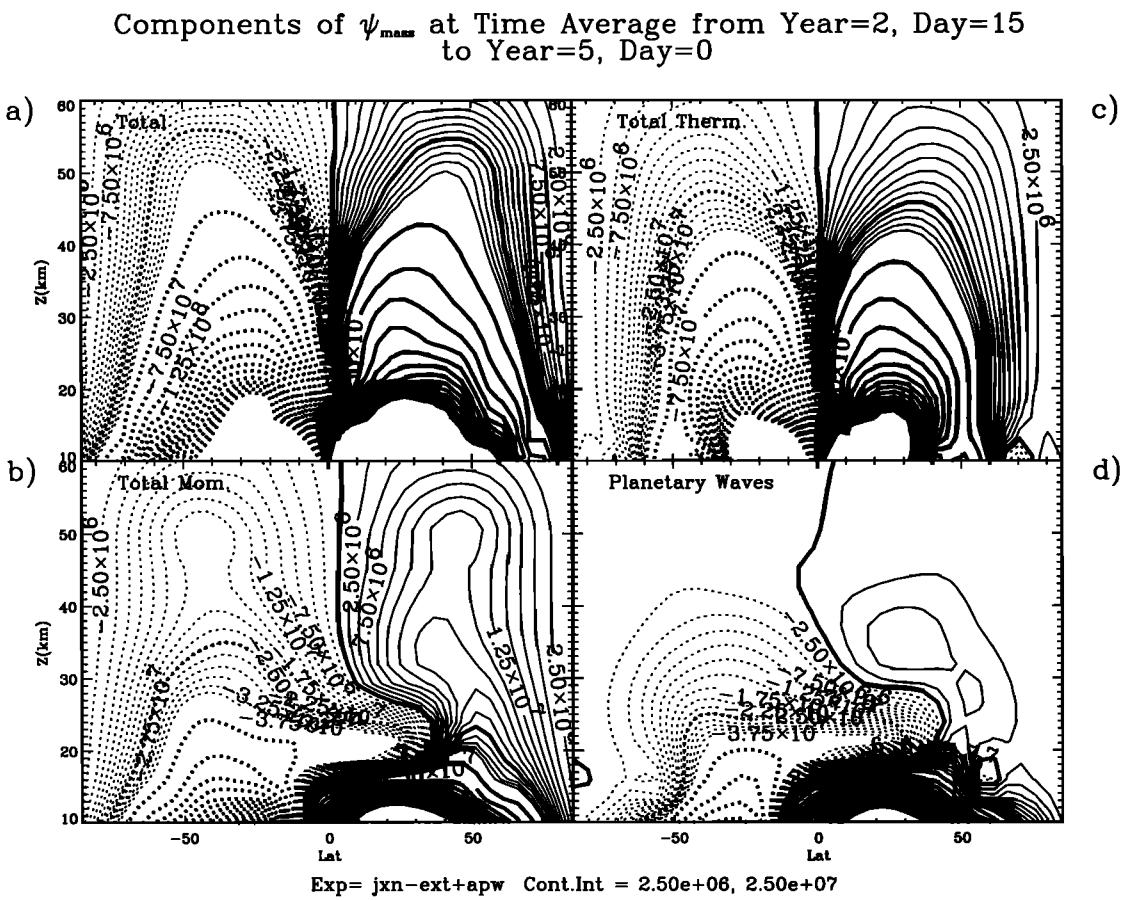

Figure 13. Three year average of mass stream function $\overline{p\psi}^t$ and components for experiment 1 ($\mathcal{H}_0$=3 K d^{-1}): (a) $\overline{p\psi}^t$ total mass streamfunction; (b) $\overline{p\psi_X}^t$ mass streamfunction forced by total mechanical forcing; (c) $\overline{p\psi_\mathcal{H}}^t$ mass streamfunction forced by total thermodynamic forcing; (d) $\overline{p\psi_{PW}}^t$ mass streamfunction forced by drag from planetary waves. Solid contours are positive and indicate a clockwise circulation. Thick contours are plotted every 2.5×10^7 mbar cm^2 s^{-1}, while thin contours are plotted every 2.5 ×10^6 mbar cm^2 s^{-1}.

tropical tropopause is modulated by extratropical drag [e.g., *Yulaeva et al.*, 1994]. However, even at 18 km in our model the annually varying component of w^* represents at most one fifth of the time-averaged w^* at the tropical tropopause. It should be pointed out again that observations indicate a larger annual cycle in tropical tropopause temperature than is present in our model, so in reality, a somewhat larger fraction of the annually averaged transport through the tropical tropopause may occur as the result of extratropical driving. In contrast, at 29 km both observations and model results indicate a weak annual cycle (<1 K) in temperature. Thus there is no a priori reason to invoke extratropical control of vertical transport at these altitudes.

4.2.3. Time-averaged stream function. From Figure 12 it is clear that in our model the dominant mode of vertical transport throughout the tropical stratosphere is advection by the time-mean portion of the vertical velocity. Both annual and semiannual variations in the model are small compared to time-mean value $<\overline{w^*}^t>_{20}$. Figure 13 shows plots of multiyear averages of the total meridional mass stream function $\overline{p\psi^*}^t$ (Figure 13a) as well as several of its components for Experiment 1. The mass stream function forced by total drag $\overline{p\psi^*_X}^t$ (Figure 13b) is shown along with that forced by total net heating $\overline{p\psi^*_\mathcal{H}}^t$ (Figure 13c). Consistent with the time series of w^*, $w^*_\mathcal{H}$, and w^*_X in Figure 12 the time-mean, total mass stream function $\overline{p\psi^*}^t$ in the tropics is dominated by $\overline{p\psi^*_\mathcal{H}}^t$. Also shown is the subcomponent of $\overline{p\psi^*_X}^t$ driven by only planetary wave EP-flux divergence $-\overline{p\psi^*_{PW}}^t$ (Figure 13d). Strong hemispheric asymmetry is evident in both $\overline{p\psi^*_X}^t$ and $\overline{p\psi^*_{PW}}^t$ as is expected for an experiment with asymmetric planetary wave forcing. However, $\overline{p\psi^*_\mathcal{H}}^t$ shows little hemispheric asymmetry, and above 20 km is more concentrated in the tropics than the drag-induced circulations. This argues against a large remote effect by extratropical planetary wave drag on the time-mean net heating of the tropical stratosphere in the present model.

Figure 14 shows the difference in these mass stream

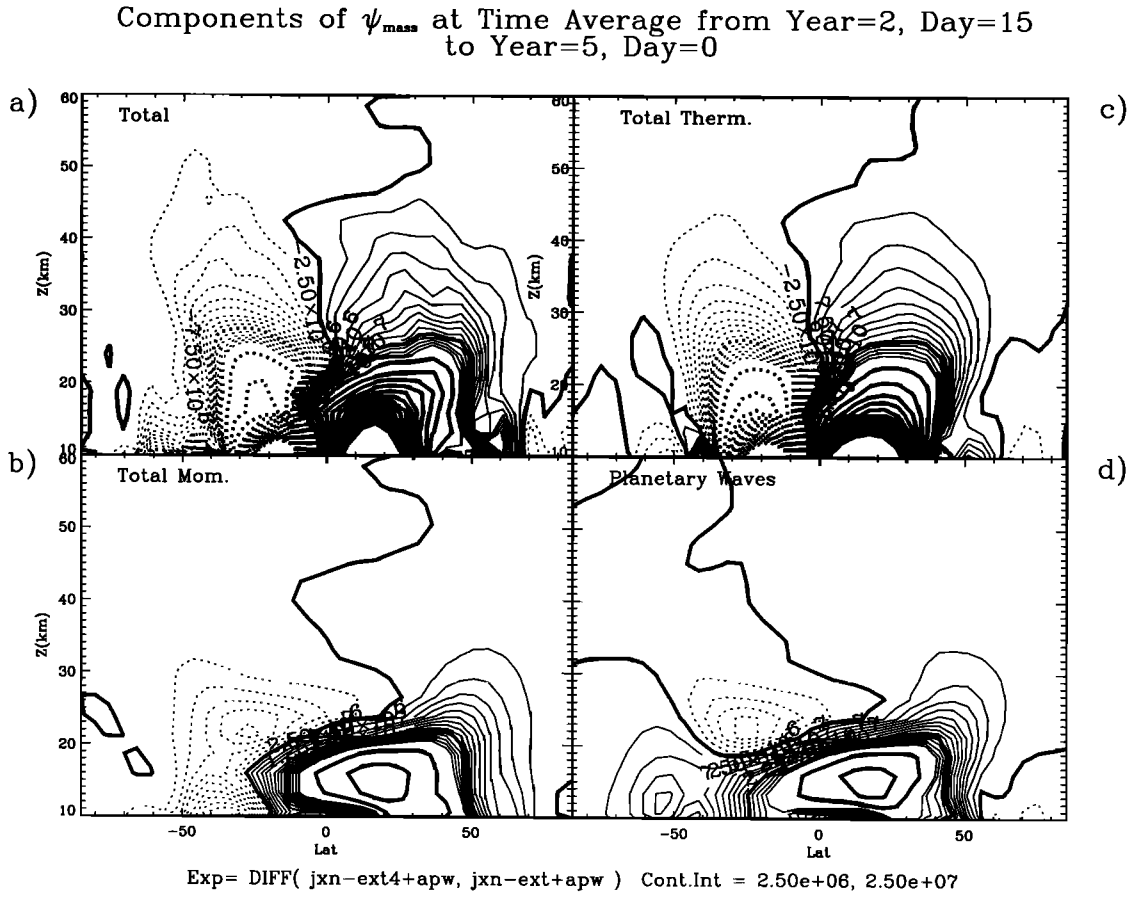

Figure 14. As in Figure 13 except that the difference in 3 year average mass streamfunction components between experiments 1 ($\mathcal{H}_0$=3 K d^{-1}) and 6 ($\mathcal{H}_0$=4 K d^{-1}) is shown. We show averaged components of $\Delta\overline{p\psi^*}^t \equiv \overline{p\psi^*}^t_{\text{Exp 6}} - \overline{p\psi^*}^t_{\text{Exp 1}}$, so positive values indicate stronger circulations in experiment 6.

function components between experiment 1 and Experiment 6. As the prescribed tropospheric heating is increased the change in mass stream function follows the pattern in Figure 13; the momentum forced components change asymmetrically, while the thermally forced component changes symmetrically about the Equator. Furthermore, the changes in $\overline{p\psi^*_X}^t$ (Figure 14b) and $\overline{p\psi^*_{PW}}^t$ (Figure 14d), while significant, are confined in the vertical and thus cannot explain the changes in $\overline{w^*}^t$ shown in Figure 11, which extend over a deep layer of the tropical stratosphere. It is these changes in w^* which lead to the sensivity of Γ to the prescribed tropospheric heating. Similar changes to $\overline{p\psi^*}^t$ and its components are observed when going to reduced tropospheric heating, i.e., between experiment 1 and experiment 5.

From the results shown in Figures 12-14 we conclude that tropical ascent in our model is controlled by tropical or at least hemispherically symmetric processes. Near tropopause altitudes the model may underestimate the influence of midlatitude planetary waves. However, if we assume the relative importance of hemispherically asymmetric planetary wave drag at the tropical tropopause can be estimated by comparing the amplitude of the annual cycle in w^* to the background floor value of w^* at 18 km in Figure 12, then even doubling the planetary wave effect will only result in an annually varying component that is at most of similar amplitude to the floor value. Doubling the amplitude of the annual oscillation in w^* at 18 km would also double the amplitude of the model's annual oscillation in tropical tropopause temperature, which is small (3 K) but within the range of observed amplitudes (Section 3.1). Doubling the amplitude of the model's annual cycle in tropical tropopause temperature would place it well within if not at the high end of the observations. Thus we conclude further that although our model may underestimate the contribution of planetary wave drag on tropical ascent at the tropopause, it does so by less than a factor of 2. At higher altitudes in tropical stratosphere we find no compelling reason to disbelieve the model's simulation of vertical motion.

4.3. Response to Lower Stratospheric Heat Source

Some of the difficulty in identifying the cause of the model's sensitivity to variations in tropospheric heating arises from the fact we expect a strong response in the

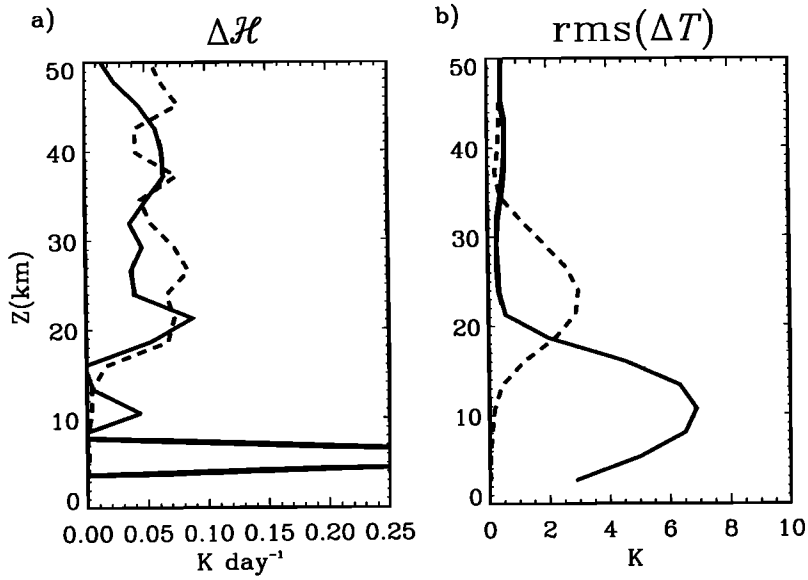

Figure 15. (a) Differences in net heating averaged over 3 model years and between 20°S and 20°N $<\overline{\mathcal{H}}^t>_{20}$ as a function of altitude. Solid curve shows net heating change between experiments 6 and 1, $<\overline{\mathcal{H}}^t>_{20\ \text{Exp}\ 6} - <\overline{\mathcal{H}}^t>_{20\ \text{Exp}\ 1}$. Dashed curve shows change between experiments 7 and 1, $<\overline{\mathcal{H}}^t>_{20\ \text{Exp}\ 7} - <\overline{\mathcal{H}}^t>_{20\ \text{Exp}\ 1}$. (b) RMS changes to temperature averaged over 3 model years and between 20°S and 20°N. Solid curve shows $<\overline{\Delta T^2}^t>_{20}^{1/2}$ for experiments 6 and 1, dashed curve shows $<\overline{\Delta T^2}^t>_{20}^{1/2}$ for experiments 7 and 1. In both instances the large values of $<\overline{\Delta T^2}^t>_{20}^{1/2}$ correspond to temperature increases in the vicinity of additional imposed heating, i.e., more imposed tropospheric heating in experiment 6 and more imposed stratospheric heating in experiment 7.

tropospheric Hadley circulation to such variations. The Hadley cell response can lead to changes in low-level zonal winds as well as in planetary wave and gravity wave generation, which can in turn modify the momentum forcing of the meridional circulation. The existence of such indirect effects on the model's atmospheric drag field is easily seen in Figure 14d where changes in prescribed tropospheric heating led to differences in the circulation forced by planetary wave EP-flux divergence. The changes in $<\overline{w^*}^t>_{20}$ with increasing $\mathcal{H}_0$ in Figure 11 are associated with small changes in the stratospheric net heating. It is of interest to see whether the circulation in the model is sensitive to direct addition of small amounts of heat to the lower stratosphere. This should leave the model's Hadley circulation relatively unaffected, while still producing changes to the stratospheric net heating similar to those resulting from changes to $\mathcal{H}_0$. Furthermore, such an experiment addresses real uncertainties in stratospheric heating which result, for example, from volcanic aerosols [e.g., *Kinne et al.*, 1992; *Kinnison et al.*, 1994; *Rosenfield et al.*, 1997].

We perform a final experiment (experiment 7) using the same value of $\mathcal{H}_0$ as in experiment 1, but with a weak additional heat source centered in the tropical lower stratosphere as shown in Figure 1b. The magnitude of this heat source, 0.3 K d^{-1}, was chosen so that the final net heating difference in the lower stratosphere was similar to that obtained between experiment 1 and experiment 6 by increasing $\mathcal{H}_0$. Figure 15a shows the difference in tropical net heating profiles $<\overline{\mathcal{H}}^t>_{20}$ between experiments 1 and 6 (solid line) and between experiments 1 and 7 (dashed line). It is clear from Figure 15 that net heating changes of 0.05 to 0.1 K d^{-1} are obtained in a deep layer of the tropical stratosphere both by increasing tropospheric heating, as in going from experiment 1 to experiment 6, or by adding heat directly to the lower stratosphere, as in experiment 7. Interestingly, the stratospheric temperature change between experiments 1 and 6 (Figure 15b) is small, implying that any increase in thermal forcing going from experiments 1 to 6 is nearly balanced by increased w^*, at least in the stratosphere. In contrast, the tropical stratosphere is 2–3 K warmer in experiment 7 than in experiment 1. This indicates that both increased IR cooling and increased w^* occur when heat is added directly to the stratosphere.

Despite the differences in stratospheric temperature profiles, the stratospheric circulations in experiments 6 and 7 are quite similar. Figures 9d and 10d show Γ and Γ^* for experiment 7 after 11 model years. There are clear similarities between these and the Γ and Γ^* distributions for experiment 6 (Figures 9c and 10c), confirming that the restricted stratospheric heat source has an overall effect on the circulation equivalent to that of simply raising $\mathcal{H}_0$.

As expected, the addition of a tropical stratospheric heat source did not affect midlatitude drag to the same

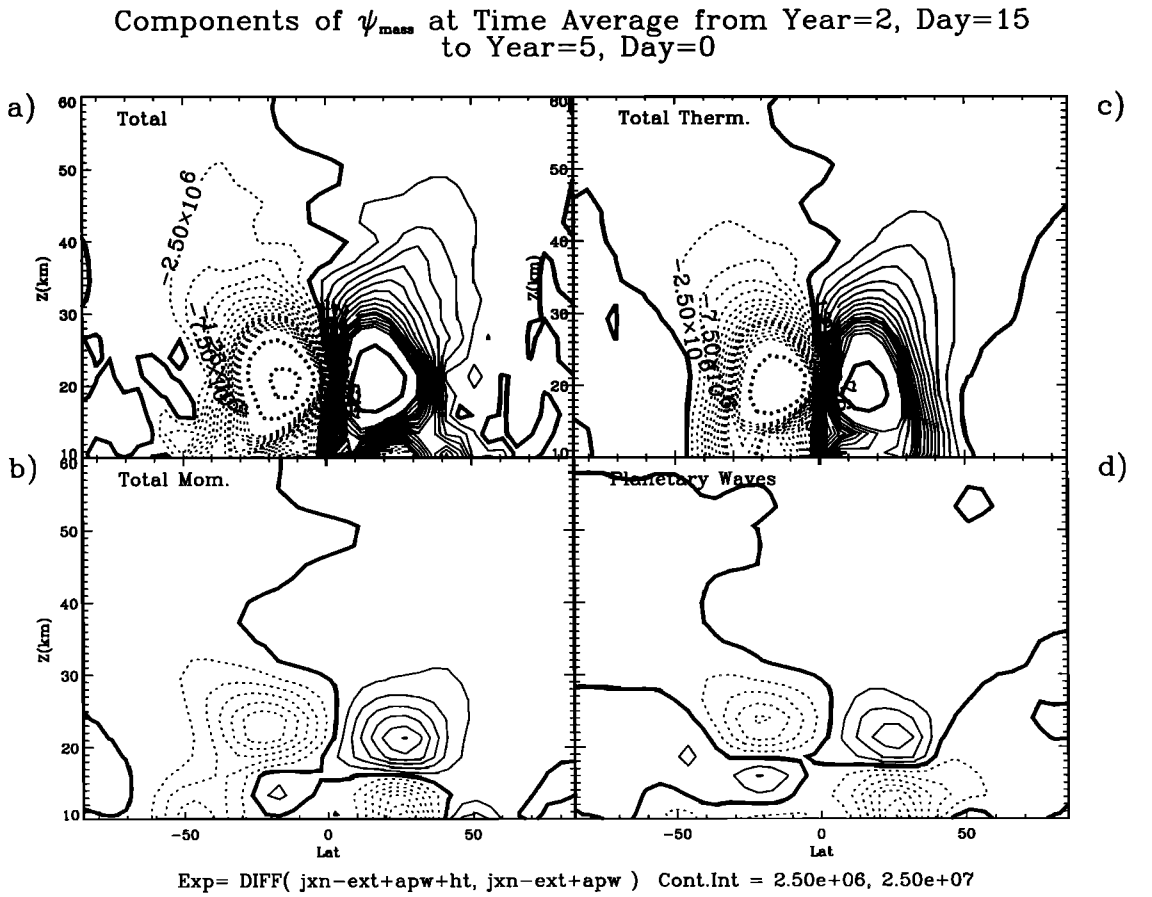

Figure 16. As in Figure 14 except for experiments 1 ($\mathcal{H}_0$=3 K d^{-1}) and 7 ($\mathcal{H}_0$=3 K d^{-1} with $\mathcal{H}_s trat$). We show averaged components of $\Delta\overline{p\psi^*}^t \equiv \overline{p\psi^*}^t_{\text{Exp 6}} - \overline{p\psi^*}^t_{\text{Exp 1}}$.

degree as an increase in $\mathcal{H}_0$. This can be seen in Figure 16 which shows the change in components of the mass stream function $\overline{p\psi^*}^t$ between experiments 1 and 7. The stratospheric changes to the total stream function $\overline{p\psi^*}^t$ and to the thermally forced component $\overline{p\psi^*_{\mathcal{H}}}^t$ (Figures 16a and 16c) are of similar magnitude and shape to those obtained between Experiments 1 and 6 (Figures 14a and 14c). Note that the changes in $\overline{p\psi^*}^t$ and $\overline{p\psi^*_{\mathcal{H}}}^t$ in Figures 16a and 16c die off rapidly below 15 km. The drag induced circulations $\overline{p\psi^*_X}^t$ and $\overline{p\psi^*_{\text{PW}}}^t$ show much weaker changes overall between Experiments 1 and 7 (Figures 16b and 16d) than were obtained between Experiments 1 and 6 (Figures 14b and 14d). Thus, the addition of a stratospheric heat source intensifies tropical vertical motion (and reduces Γ) without creating a significant change to the circulation forced by midlatitude drag.

The sensitivity of our model's circulation and Γ to tropospheric heating variations must be viewed with caution due to the incomplete tropospheric dynamics in the model. However, the response of the model to the restricted stratospheric heat source given by (4d) was obtained without appreciable effects in the model troposphere. The ~0.10 K d^{-1} net heating change induced by the stratospheric heat source (Figure 15a) is also well within the possible perturbations induced by a major volcanic eruption.

We have not yet isolated the mechanism responsible for increasing our model's tropical vertical velocities as $\mathcal{H}_0$ increases. However, the analysis shown here indicates that (1) midlatitude wave drag is not involved, and (2) similar effects on w^* can be induced by a purely stratospheric heat source. There are at least two possibilities which have not been addressed here. (1) Tropospheric temperature increases as $\mathcal{H}_0$ grows (Figure 15b), are "seen" by the stratosphere and produce local increases in stratospheric net heating. (2) Increased w^* in the lower stratosphere is remotely forced by increased $\mathcal{H}_{\text{latent}}$. Either of these mechanisms could be reinforced by secondary circulations arising from the initial changes to the lower stratospheric net heating. A complete examination of these possibilities is beyond the scope of the present paper.

5. Summary and Discussion

This study examined factors controlling age of air in a 2-D, zonally averaged model of the atmosphere. We examined age distributions derived from two tracers.

The forcing and evolution of both tracers were identical in each model simulation except that one tracer was affected by horizontal mixing while the other was not. Comparisons of mixed age (Γ) and unmixed age (Γ^*) in our simulations reveal qualitative as well as quantitative differences. In all of the simulations, Γ^* was 1 to 2 years less than Γ in most of the middle atmosphere. The polar lower stratosphere was the only region of the atmosphere in which Γ^* was larger than Γ. We found a systematic sensitivity of Γ^* to the strength of prescribed tropical tropospheric heating in the model. As the peak strength of the prescribed heating increased from 2 K d^{-1} to 4 K d^{-1}, with fixed planetary wave forcing, the typical middle atmospheric value of Γ^* decreased from around 2.5 to less than 1.7 years (Figure 10). In contrast, when prescribed tropospheric heating was fixed and planetary wave forcing amplitudes were varied from 125 m to 350 m, little change was noted in Γ^* (Figure 6). Thus, Γ^* (and w^*) in our model was sensitive to changes in prescribed tropospheric heating but not to changes in planetary wave forcing amplitudes.

Mixed age Γ was found to be sensitive to changes in both prescribed tropospheric heating and planetary wave forcing amplitudes. As planetary wave forcing amplitudes were increased from 125 to 350 m, K_{yy} in the lower stratosphere increased by a factor of 8 (Figure 8). This stronger mixing resulted in increased values of Γ in the middle atmosphere for larger planetary wave forcing even though Γ^* stayed relatively constant (Figure 6). Stronger vertical motion in the tropics also led to lower values of Γ as $\mathcal{H}_0$ increased (Figure 9). A comparison of Γ with atmospheric observations yielded reasonable agreement for $\mathcal{H}_0$=2 or 3 K d^{-1}. Our peak lower stratospheric age of ~6 years in experiment 5 ($\mathcal{H}_0$=2 K d^{-1}) agrees with age estimates based on balloon-borne CO_2 [*Schmidt and Khedim*, 1991] but is substantially less than the very high values of 8 to 10 years obtained by *Harnisch et al.* [1996] from their balloonborne SF_6 measurements. Our upper stratospheric Γ values of 4 to 5 years for $\mathcal{H}_0$=2 and 3 K d^{-1} were also somewhat below the 5.9 year age estimate from HALOE HF* [*Russell et al.*, 1996]. Finally, using $\mathcal{H}_0$=2 K d^{-1}, we obtain reasonable agreement with the 3-D MACCM2 age simulations of *Waugh et al.* [1997] using the updated gravity wave parameterization (MACCM2 version 2).

The high values of midstratospheric Γ (>5 years) obtained from gases with linearly increasing tropospheric sources (e.g., HF, CO_2, SF_6) are much longer than the transit times of tropical water vapor pulses in HALOE and MLS observations of (i.e., the atmospheric "tape recorder"). These pulses travel from 15 km to 35 km in approximately 1.2 – 1.5 years (see Plate 1; or *Mote et al.*, [1996, Plate 1]). *Mote et al.* [1996] show that the minima and maxima of zonally averaged tropical water vapor approximately trace the path described by a Lagrangian parcel in the mean meridional circulation. The transit time of such pulses may be a better approximation of the modal time (or peak) of the age spectrum than its first moment Γ, which corresponds to "age" derived from long-lived tracers [*Hall and Waugh*, 1997]. The time evolution of the unmixed age tracer μ^* in the tropics (Plate 1) shows that with $\mathcal{H}_0$=2 K d^{-1} and $\mathcal{H}_0$=3 K d^{-1}, our model does a good job of reproducing the apparent vertical trajectories of pulses in $2CH_4+H_2O$ observed by HALOE. Thus simulations with these values of $\mathcal{H}_0$ quantitatively reproduce both the high values of Γ estimated for the midstratosphere using trace gas mixing ratios and the apparent configuration of tropical ascent inferred from HALOE and MLS water vapor observations. This indicates that our model correctly simulates the balance between vertical advection and horizontal tropical/midlatitude exchange which characterizes tracer transport in the tropical stratosphere [e.g., *Plumb*, 1996; *Volk et al.*, 1996; *Minschwaner et al.*, 1996]. Put another way, these results show that our simulations with $\mathcal{H}_0$=2 K d^{-1} and $\mathcal{H}_0$=3 K d^{-1} reproduce both the first moment and the peak of the atmospheric age spectrum. It is gratifying that a correct simulation of these processes is associated with planetary wave and tropospheric heating parameters that also yield reasonable simulations of stratospheric zonal winds and temperatures in the model.

The sensitivity of Γ and Γ^* in our model to prescribed tropical tropospheric heating $\mathcal{H}_0$ is due to vertical velocities in the tropical stratosphere, which exhibited a larger than expected senstivity to $\mathcal{H}_0$, while exhibiting little if any sensitivity to changes in planetary wave forcing amplitudes. Changes to $\mathcal{H}_0$ can affect the global distribution of either drag or net heating, both of which could impact the meridional circulation. By decomposing the total residual stream function into separate components associated with drag X and net heating $\mathcal{H}$, we showed that changes in the tropical vertical velocity are not forced by changes to the model planetary wave drag. We found that the total residual stream function above 25 km in the tropics was dominated by the contribution from the heating. Furthermore, even though hemispherically asymmetric planetary wave forcing was used, we found that the change to the residual stream function as $\mathcal{H}_0$ varied remained relatively symmetric. These facts indicate that varying the prescribed tropospheric heating in our model alters tropical ascent primarily by an upward directed change to the net heating of the tropical lower stratosphere, rather than by an indirect, mechanically-forced path mediated by midlatitude drag.

The tropospheric response of our 2-D, zonally averaged model to changes in heating is severely limited by exclusion of baroclinic instability and explicit water vapor cycles. Therefore the sensitivity of Γ to $\mathcal{H}_0$ may be primarily a model tuning issue. However, we also found that Γ is sensitive to a small, directly imposed, stratospheric heat source. A small ~0.3 K d^{-1} heat source confined to the tropical lower stratosphere (Figure 1b) had effects on both Γ and w^*, similar to those obtained by raising the tropospheric heating from 3 to 4 K d^{-1}. Variations of 0.1– 0.3 K d^{-1} in stratospheric net heating such as obtained in experiment 7 (Figure 14) are well within the range of current uncertainties. It has been shown, for example, that tropical lower stratospheric

net heating rates are particularly sensitive to details in the treatment of surface albedo, tropospheric clouds, as well as to secondary radiatively active species such as N_2O, NO_2, CH_4, and O_2 [*Eluszkiewicz et al.*, 1996]. Furthermore, the stratospheric aerosol load produced by major volcanic eruptions can perturb net heating rates by 0.2-0.5 K d^{-1} [*Kinne*, 1992; *Kinnison et al.*, 1994; *Eluszkiewicz et al.*, 1996].

Thus our results suggest that variability in stratospheric net heating may be a significant contributor to observed variations in upward motion in the tropics. Such variability may have to be considered as a possible explanation for interannual variations in the rate of vertical transport in the lower stratosphere, along with the variations introduced by the quasi-biennial oscillation [*Mote et al.*, 1996; *Randel et al.*, 1996]. A possible connection between age and changes in diabatic heating was made earlier by *Schmidt and Khedim* [1991] to explain a 3 to 5 year periodicity in values of age determined from balloon borne measurements of CO_2. Variations in factors such as cloud cover, surface albedo, or actual tropical tropospheric temperatures may be related to El Niño/Southern–Oscillation (ENSO). Schmidt and Khedim speculated that ENSO-related effects acting on the meridional circulation could induce the 3 to 5 year periodicity they observe in age. Volcanic aerosols vary in an unpredictable manner, but their potential impact is large. Volcanic aerosols from Pinatubo were present in the lower stratosphere during much of the early UARS observation period [e.g., *Kinne et al.*, 1992; *Kinnison et al.*, 1994]. So variations in ascent rates may be present in the UARS HALOE and MLS data as result of this changing stratospheric aerosol load.

Appendix: Idealized Response to a Steady Momentum Source

In the TEM formulation the thermal wind relation is used with (1a) and (1b) to form a diagnostic elliptic equation for the residual meridional stream function ψ^*,

$$\mathrm{Ell}(\psi^*) = -\left(f + \frac{2\overline{U}\tan\phi}{a}\right)\frac{\partial}{\partial z}X + RH^{-1}e^{-\kappa z/H}\frac{\partial}{a\partial\phi}\mathcal{H} - \frac{\partial}{\partial t}\epsilon \quad \text{(A1)}$$

where the symbol Ell() denotes a complicated elliptic operator, which depends on $\overline{U}$ and $\overline{\theta}$ as well as other zonal mean quantities. The term $\partial_t\epsilon$ in (A1) represents departures from geostrophic balance, which are parameterized as discussed by *Bacmeister et al.* [1995]. The component stream functions ψ^*_X and $\psi^*_{\mathcal{H}}$ and associated velocities discussed in section 4 are simply derived from truncated versions of (A1), where only one or a subset of the forcing terms on the RHS has been retained, for example,

$$\mathrm{Ell}(\psi^*_X) = -\left(f + \frac{2\overline{U}\tan\phi}{a}\right)\frac{\partial}{\partial z}X.$$

While these stream function components contain no information that is not already present in their source terms, they offer a straightforward and physically meaningful way to assess the relative importance of the numerous drag and heating mechanisms in a 2-D model.

In this Appendix we will use stream function components to examine the zonally averaged response of an idealized atmosphere to a localized source of momentum [e.g., *Haynes et al.*, 1991; *Holton et al.*, 1995]. Haynes et al. showed that for a steady momentum source the mean meridional mass circulation approaches a steady state in which the circulation is confined along lines of constant angular momentum below the forcing. This configuration of momentum forcing and residual circulation has been called "downward control." Here we will show how downward control is established by a reactive, thermally driven circulation, which arises in response to temperature changes brought about by the initial mechanically forced circulation.

We specify a time independent momentum forcing given by

$$X = A_{\mathrm{Force}}\exp\left[-\left(\frac{\phi-\phi_{\mathrm{Force}}}{\Delta\phi_{\mathrm{Force}}}\right)^2\right] \times \exp\left[-\left(\frac{z-z_{\mathrm{Force}}}{\Delta z_{\mathrm{Force}}}\right)^2\right] \quad \text{(A2)}$$

The peak amplitude of the steady momentum forcing A_{Force} is chosen to be 5 m $s^{-1}d^{-1}$ and the center of the forcing is chosen to be at z=45 km and ϕ=45°N. The scales for the forcing are set to $\Delta z_{\mathrm{Force}}$=10 km and $\Delta\phi_{\mathrm{Force}}$=10°. The net heating $\mathcal{H}$ is given by simple Newtonian cooling to a latitude independent, reference temperature profile

$$\mathcal{H} = \frac{\overline{\theta}(\phi,z,t) - \overline{\theta}_{\mathrm{Global}}(z)}{\tau_{\mathrm{Newt}}} \quad \text{(A3)}$$

The relaxation time τ_{Newt} is constant with latitude and height and is chosen to be 4 days. Parameters in (A2) and (A3) are chosen to be similar to those used by *Haynes et al.* [1991].

Figure 17 shows the evolution of the meridional mass stream function after the constant momentum forcing (A2) is turned on at t=0 in an atmosphere initially at rest. The top row of panels shows the time evolution of the total mass stream function $\rho\psi^*$, with time increasing from left to right. The middle row shows the time evolution of $\rho\psi^*_X$ (the component due to the momentum forcing), and the bottom row shows the time evolution of $\rho\psi^*_{\mathcal{H}}$ (the component forced by thermal relaxation). In these plots a maximum in $\rho\psi^*$ implies clockwise circulation. Early in the simulation (after 6 days) the total mass stream function $\rho\psi^*$ is close to $\rho\psi^*_X$, implying essentially a single clockwise cell with a broad ascending branch on the equatorward flank and a more concentrated descending branch on the poleward flank. The initial, thermally forced circulation $\rho\psi^*_{\mathcal{H}}$ is weak. However, as time progresses, the temperature field is displaced farther from its initial equilib-

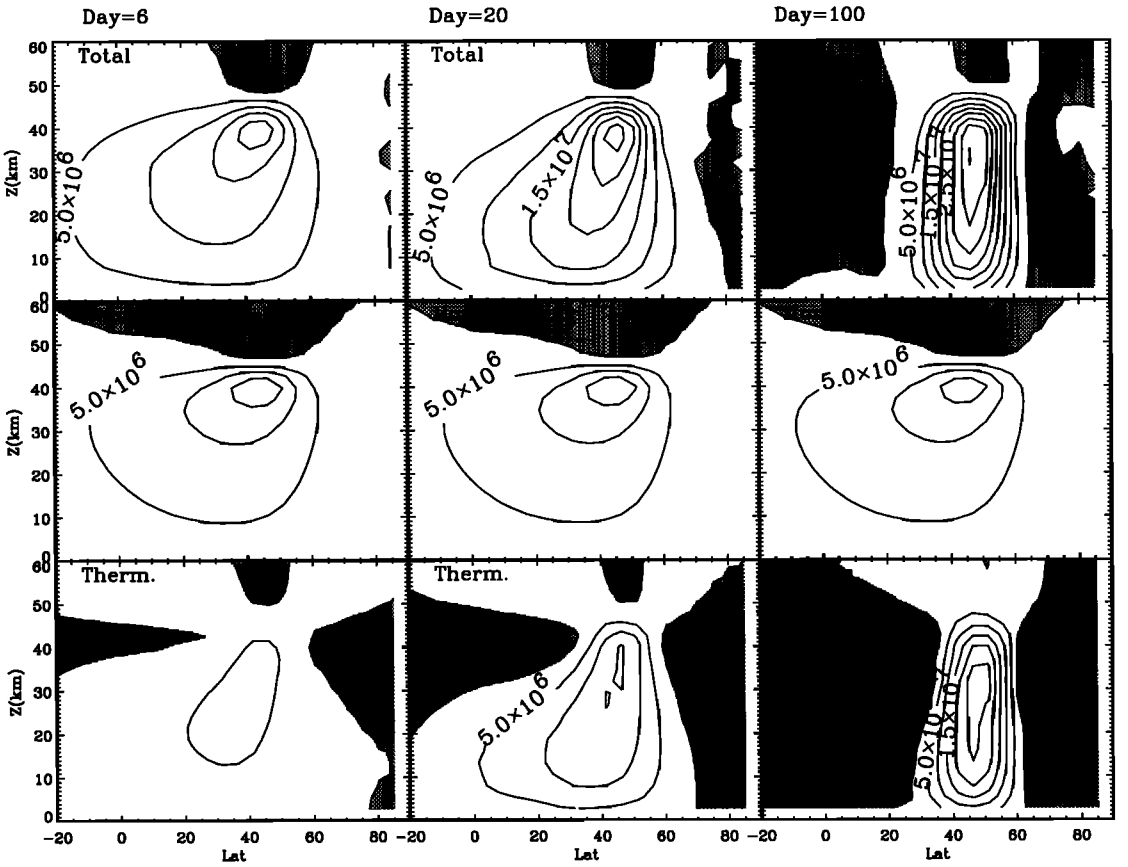

Figure 17. Residual mass stream functions $p\psi$ for idealized experiment described in the Appendix. Constant body force centered at 45°N and 45 km is applied starting at day zero. Thermal forcing is limited to Newtonian cooling to reference temperature profile with a time constant of 4 days. Top row shows total mass stream function $p\psi_X$. Middle row shows mass stream function forced by mechanical forcing alone, $p\psi_X$. Bottom row shows mass stream function forced by thermal forcing alone, $p\psi_{\mathcal{H}}$. Left-hand column shows the three mass stream functions on day 6, middle column on day 20, and right-hand column on day 100.

rium state. The relaxational thermodynamic forcing $\mathcal{H}$ becomes stronger as does the thermally forced circulation $\rho\psi^*_{\mathcal{H}}$. The thermally forced circulation consists of a multiple cell pattern with a strong, horizontally localized clockwise cell below the forcing, a counterclockwise cell developing on the equatorward flank of the central cell, and a third weaker counterclockwise cell developing on the poleward flank.

Eventually, as steady state is achieved, the total mass stream function $\rho\psi^*$ approaches the "downward control" configuration discussed by *Haynes et al.* [1991], with motion largely confined below the momentum forcing. This can be seen in the top right-hand panel of Figure 17, which shows $\rho\psi^*$ after 100 days. However, the approach to the steady state, downward controlled configuration is achieved by intensification of the thermally forced circulation $\rho\psi^*_{\mathcal{H}}$, which remains highly nonlocal. Horizontal localization ("downward control") occurs because $\rho\psi^*_{\mathcal{H}}$ almost exactly cancels $\rho\psi^*_X$ outside of the region below the constant momentum forcing. Throughout the simulation, $\rho\psi^*_X$ remains approximately constant in time (Figure 17, middle row). The small differences in $\rho\psi^*_X$ between day 6 and day 100 are due to changes in the coefficients of the linear elliptic operator in (A1) which result as $\overline{U}$ and $\overline{\theta}$ evolve with time. Nevertheless, in the final steady state both $\rho\psi^*_X$ and $\rho\psi^*_{\mathcal{H}}$ remain highly nonlocal and only their sum exhibits the horizontal localization required of the state steady solution by the downward control principle.

Clearly, in the simulation just described, it is physically meaningful to speak of a primary residual circulation associated with momentum forcing and a secondary or reactive circulation associated with thermodynamic forcing/relaxation. For downward control to exist, the secondary circulation must be equal and opposite to the primary circulation in regions horizontally away from the steady momentum source. Thus the eventual magnitude of the secondary thermal circulation in these locations is completely determined by the circulation associated with the momentum forcing. Immediately below the imposed momentum forcing, the situation is more complicated, $\rho\psi^*_{\mathcal{H}}$ becomes more intense than $\rho\psi^*_X$. Thus the total stream function below the imposed forcing winds up closer in magnitude and

shape to the thermally forced stream function, despite the fact that its ultimate "cause" is the mechanically forced circulation in the middle row of Figure 17.

An implication of the simulation in Figure 17 is that for relaxational net heating the adiabatic response to a distant momentum source represents a reasonable estimate of the maximum impact that momentum source can have on the local circulation. In other words, the thermally reactive circulation (Figure 17, bottom row) will be at most of a similar magnitude to the adiabatic response (Figure 17, middle row) horizontally well away from the momentum forcing. Thus it seems reasonable to use the adiabatic stream function response to a given momentum forcing to assess the magnitude of its possible remote effects. We would argue therefore that the small contribution of w_X^* to the total vertical velocity in the tropical stratosphere (Figure 12), argues against a significant impact by midlatitude drag.

Information obtained by decomposing the stream function into components does not contradict results obtained by steady state reasoning where steady state conditions apply. In the example just examined, the final net heating away from the imposed momentum source approaches zero, so that $w^* = 0$ there is consistent with the steady state solution. However, the zero-motion state away from the momentum forcing is achieved by two nonzero circulations associated with the thermal forcing and the momentum forcing of the elliptic equation (A1). Examining component streamfucntions may be helpful in situations where forcings vary with time and relaxational time constants are difficult to determine. Furthermore, even in steady state situations, component stream functions may be helpful in evaulating the sensitivity of circulations to changes in heating and drag parameters.

Acknowledgments. The authors thank Bob Conway for his support and encouragment. JTB appreciates useful discussions with Mark Schoeberl, as well as careful reviews by Tim Hall and an anonymous reviewer, all of which led to substantial improvements in this paper. This work was supported by the Office of Naval Research, NASA contract W-18,566, and NASA's UARS Guest Investigator Program.

References

Andrews, D. G., J. R. Holton and C. B. Leovy, *Middle Atmosphere Dynamics*,489 pp., Academic Press, San Diego, Calif., 1987.

Bacmeister, J. T., Mountain-wave drag in the stratosphere and mesosphere inferred from observed winds and a simple mountain-wave parameterization scheme, *J. Atmos. Sci.*, 50, 377-399, 1993.

Bacmeister, J. T., M. R. Schoeberl, M. E. Summers, J. R. Rosenfield, and X. Zhu, Descent of long-lived trace gases in the winter polar vortex, *J. Geophys. Res., 100,* 11,669-11,684, 1995.

Bischof, W., R. Borchers, P. Fabian, and B. C. Krüger, Increased concentration and vertical distribution of carbon dioxide in the stratosphere, *Nature, 316,* 708-710 1985.

Boering, K. A., et al., CO_2 and N_2O correlations during SPADE, *Geophys. Res. Lett., 21,* 2567-2570, 1994.

Boering, K. A., et al., Measurements of carbon dioxide and water vapor at northern midlatitudes: Implications for troposphere-to-stratosphere exchange, *Geophys. Res. Lett., 22,* 2737-2740, 1995.

Elkins, J. W., et al., Airborne gas chromatograph for in situ measurements of long-lived species in the upper troposphere and lower stratosphere, *Geophys. Res. Lett., 23,* 347-350, 1996.

Eluszkiewicz, J., et al., Residual circulation in the stratosphere and lower mesosphere as diagnosed from Microwave Limb Sounder data, *J. Atmos. Sci., 53,* 217-240, 1996.

Fleming, E. L., S. Chandra, M. R. Schoeberl, and J. J. Barnett, Monthly mean global climatology of temperature, wind, geopotential height, and pressure for 0-120 km, NASA Tech. Memo. *100697,* 85 pp., 1988.

Garcia, R. R., Parameterization of planetary wave breaking in the middle atmosphere, *J. Atmos. Sci., 48,* 1405-1419, 1991.

Garcia, R. R., F. Stordal, S. Solomon, and J. T. Kiehl, A new numerical model of the middle atmosphere, 1, Dynamics and transport of tropospheric source gases, *J. Geophys. Res., 97,* 12,967-12,992, 1992.

Garcia, R. R., T. J. Dunkerton, R. Lieberman, and R. A. Vincent, Climatology of the semiannual oscillation of the tropical middle atmosphere, *J. Geophys. Res., 102,* 26,019–26,032, 1997.

Hall, T. M., and D. W. Waugh, Timescales for the stratospheric circulation derived from tracers, *J. Geophys. Res., 102,* 8991-9001, 1997.

Hall, T. M., and R. A. Plumb, Age as a diagnostic of stratospheric transport, *J. Geophys. Res., 99,* 1059-1070, 1994.

Hall, T. M., and M. J. Prather, Simulations of the trend and annual cycle in stratospheric CO_2, *J. Geophys. Res., 98,* 10,573-10,581, 1993.

Harnisch, J., R. Borchers, P. Fabian, and M. Maiss, Tropospheric trends for CF_4 and C_2F_6 derived from SF_6 dated stratospheric air, *Geophys. Res. Lett., 23,* 1099-1102, 1996.

Haynes, P. H., C. J. Marks, M. E. McIntyre, T. G. Shepherd, and K. P. Shine, On the "downward control" of extratropical diabatic circulations by eddy-induced mean zonal forces, *J. Atmos. Sci., 48,* 651-678, 1991.

Holton, J. R., P. H. Haynes, M. E. McIntyre, A. R. Douglass R. B. Rood, and L. Pfister, Stratosphere-troposphere exchange, *Rev. Geophys., 33,* 403-439, 1995.

Iwasaki, T., General circulation diagnosis in the pressure-isentrope hybrid vertical coordinate, *J. Meteorol. Soc. Jpn., 70,* 673-687, 1992.

Kinne, S., O. B. Toon, and M. J. Prather, Buffering of the stratospheric circulation by changing amounts of tropical ozone: A Pinatubo case study, *Geophys. Res. Lett., 19,* 1927-1930, 1992.

Kinnison, D. E., K. E. Grant, P. S. Connel, D. A. Rottman, and D. J. Wuebbles, The chemical and radiative effects of the Mount Pinatubo eruption, *J. Geophys. Res., 99,* 25,705-25,731, 1994.

McIntyre, M. E., and T. N. Palmer, Breaking planetary waves in the stratosphere, *Nature, 328,* 590-596, 1983.

Minschwaner, K. A., A. E. Dessler, J. W. Elkins, C. M. Volk, D. W. Fahey, M. Loewenstein, J. R. Podolske, A. E. Roche, and K. R. Chan, The bulk properties of isentropic mixing into the tropics of the lower stratosphere, *J. Geophys. Res., 101,* 9433-9439, 1996.

Mote, P. W., K. H. Rosenlof, J. R. Holton, R. S. Harwood, and J. W. Waters, Seasonal variations of water vapor in the tropical lower stratosphere, *Geophys. Res. Lett., 22,* 1093-1096, 1995.

Mote, P. W., K. H. Rosenlof, M. E. McIntyre, E. S. Carr, J. C. Gille, J. R. Holton, J. S. Kinnersley, H. C. Pumphrey, J. M. Russell, and J. W. Waters, An atmospheric tape

recorder: The imprint of tropical tropopause temperature on stratospheric water vapor, *J. Geophys. Res., 101,* 3989-4006, 1996.

Newell, R. E., and S. Gould-Stewart, A stratospheric fountain? *J. Atmos. Sci., 38,* 2789-2796, 1981.

Newell, R. E., D. G. Vincent, T. G. Dopplick, D. Ferruza, and J. W. Kidson, The energy balance of the global atmosphere, in *The Global Circulation of the Atmosphere,* edited by G. A. Corby, pp. 42-90, R. Meteorol. Soc., London, 1970.

Peixoto, J. P., and A. H. Oort, *Physics of Climate,* 520 pp., Am. Inst. of Phys., New York, 1992.

Pierce, R. B., T. D. Fairlie, W.J. Grose, R. Swinbank, and A. O'Neill, Mixing processes within the polar night jet, *J. Atmos. Sci., 51,* 2957-2972, 1994.

Plumb, R. A., A "tropical pipe" model of stratospheric transport, *J. Geophys. Res., 101,* 3957-3972, 1996.

Plumb, R. A., and M. K. W. Ko, Interrelationships between mixing ratios of long-lived stratospheric constituents, *J. Geophys. Res., 97,* 10,145-10,156, 1992.

Prather, M. J., Numerical advection by conservation of second order moments, *J. Geophys. Res., 91,* 6671-6681, 1986.

Randel, W. J., Global atmospheric circulation statistics, 1000–1 mbar, NCAR Tech. Note 366+STR, 256 pp., Natl. Cent. for Atmos. Res., Boulder, Colo., 1992.

Randel, W. J., F. Wu, J. M. Russell, and A. Roche, Seasonal cycles and QBO variations in stratospheric CH_4 and H_2O observed in UARS HALOE data, submitted to *J. Atmos. Sci.*, 1996.

Rood, R. B., Numerical advection algorithms and their role in atmospheric transport and chemistry models, *Rev. Geophys., 25,* 71-100, 1987.

Rosenfield, J. R., D. B. Considine, P. E. Meade, J. T. Bacmeister, C. H. Jackman, and M. R. Schoeberl, Stratospheric effects of the Mount Pinatubo aerosol studied with a coupled two-dimensional model, *J. Geophys. Res., 102,* 3649-3670, 1997.

Rosenlof, K. H., Seasonal cycle of the residual mean meridional circulation in the stratosphere, *J. Geophys. Res., 100,* 5173-5191, 1995.

Rosenlof, K. H., and J. R. Holton, Estimates of the stratospheric residual circulation using the downward control principle, *J. Geophys. Res., 98,* 10,465-10,479, 1993.

Russell, J. M., M. Luo, R. J. Cicerone, and L. E. Deaver, Sattelite confirmation of the dominance of chlorofluorocarbons in the global stratospheric chlorine budget, *Nature, 379,* 6565, 1996.

Schmidt, U., and A. Khedim, In situ measurements of carbon dioxide in the winter arctic vortex and at midlatitudes: An indicator of the 'age' of stratospheric air, *Geophys. Res. Lett., 18,* 763-766, 1991.

Shia, R. L., Y. L. Ha, J. S. Wen, and Y. L. Yung, Two-dimensional atmospheric transport and chemistry model: Numerical experiments with a new advection algorithm, *J. Geophys. Res., 95,* 7467-7483, 1990.

Siskind,, D. E., J. T. Bacmeister, M. E. Summers, S. E. Zazadil, and J. M. Russell, Two dimensional model calculations of nitric oxide transport in the middle atmosphere and comparison with HALOE data, *J. Geophys. Res., 102,* 3527-3545, 1997.

Summers, M. E., D. E. Siskind, J. T. Bacmeister, R. R. Conway, S. E. Zazadil, and D. F. Strobel, The seasonal variation of middle atmosphere CH_4 and H_2O with a new chemical dynamical model, *J. Geophys. Res., 102,* 3503-3526, 1997.

Volk, C. M., et al., Quantifying transport between the tropical and mid-latitude lower stratosphere, *Science, 272,* 1763-1768, 1996.

Waugh, D. W., et al., Three-dimensional simulations of long-lived tracers using winds from MACCM2, *J. Geophys. Res., 102,* 21,493–21,513, 1997.

Yulaeva, E., J. R. Holton, and J. M. Wallace, On the cause of the annual cycle in the tropical lower stratospheric temperature, *J. Atmos. Sci., 51,* 169-174, 1994.

J. T. Bacmeister, D. E. Siskind, and M. E. Summers, Naval Research Laboratory, Code 7641, Washington, D. C. 20375. (e-mail: julio@ismap5.nrl.navy.mil)

S. D. Eckermann, Computational Physics Inc., 2750 Prosperity Ave., Fairfax, VA 22031.

(Received January 14, 1997; revised December 24, 1997; accepted December 30, 1997)